Short article

Cell Host & Microbe

Virological characteristics of the SARS-CoV-2 BA.2.86 variant

Graphical abstract

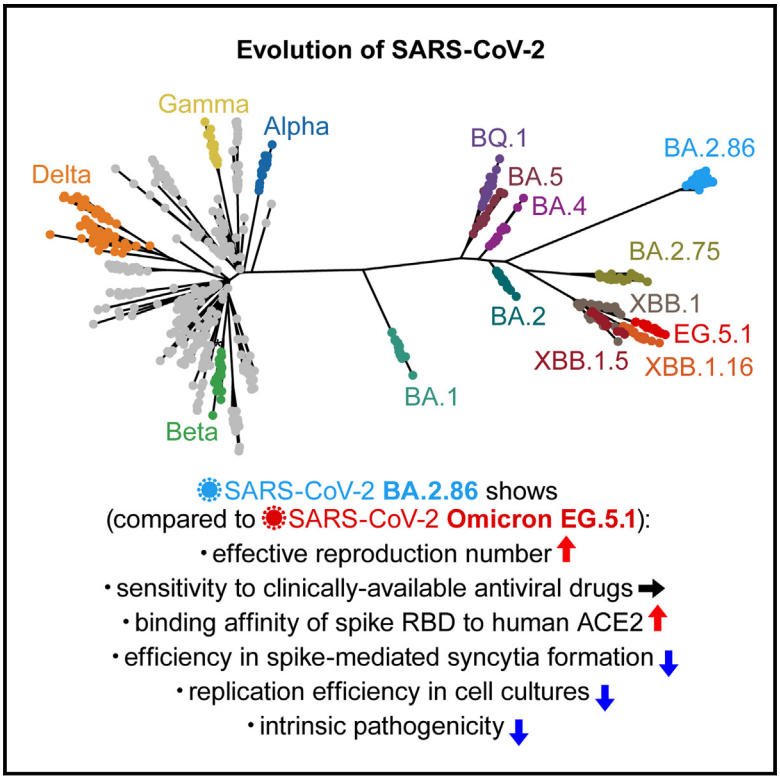

Highlights

- BA.2.86 is more transmissible than the currently predominant EG.5.1
- The sensitivity of BA.2.86 to antiviral drugs is comparable to that of EG.5.1
- The replication efficiency of BA.2.86 *in vitro* and *in vivo* is lower than that of EG.5.1
- In hamsters, BA.2.86 is less pathogenic than EG.5.1 and the parental BA.2

Authors

Tomokazu Tamura, Keita Mizuma, Hesham Nasser, ..., Keita Matsuno, Takasuke Fukuhara, Kei Sato

Correspondence

tanaka@med.hokudai.ac.jp (S.T.), jiri.zahradnik2@gmail.com (J.Z.), ikedat@kumamoto-u.ac.jp (T.I.), kazuo.takayama@cira.kyoto-u.ac.jp (K.T.), matsuk@czc.hokudai.ac.jp (K.M.), fukut@pop.med.hokudai.ac.jp (T.F.), keisato@g.ecc.u-tokyo.ac.jp (K.S.)

In brief

Tamura and G2P-Japan Consortium et al. elucidate the virological properties of the SARS-CoV-2 BA.2.86 variant. BA.2.86 is more transmissible than EG.5.1. Although the BA.2.86 spike has higher ACE2 affinity, it is less fusogenic and less replicative than the EG.5.1 spike. Notably, BA.2.86 is less pathogenic than EG.5.1 and BA.2.

Tamura et al., 2024, Cell Host & Microbe *32*, 170–180
February 14, 2024
https://doi.org/10.1016/j.chom.2024.01.001

CellPress

CellPress
OPEN ACCESS

Cell Host & Microbe

Short article

Virological characteristics of the SARS-CoV-2 BA.2.86 variant

Tomokazu Tamura,[1,2,3,4,5,6,33] Keita Mizuma,[7,33] Hesham Nasser,[8,9,33] Sayaka Deguchi,[10,33] Miguel Padilla-Blanco,[11,12,33] Yoshitaka Oda,[13,33] Keiya Uriu,[14,15,33] Jarel E.M. Tolentino,[14,16,33] Shuhei Tsujino,[1] Rigel Suzuki,[1,2] Isshu Kojima,[7] Naganori Nao,[2,3,17] Ryo Shimizu,[8] Lei Wang,[13,18] Masumi Tsuda,[13,18] Michael Jonathan,[8] Yusuke Kosugi,[14,15] Ziyi Guo,[14] Alfredo A. Hinay, Jr.,[14] Olivia Putri,[14,19] Yoonjin Kim,[14,20] Yuri L. Tanaka,[21] Hiroyuki Asakura,[22]

(Author list continued on next page)

[1]Department of Microbiology and Immunology, Faculty of Medicine, Hokkaido University, Sapporo, Japan
[2]Institute for Vaccine Research and Development (IVReD), Hokkaido University, Sapporo, Japan
[3]One Health Research Center, Hokkaido University, Sapporo, Japan
[4]Graduate School of Medicine, Hokkaido University, Sapporo, Japan
[5]School of Medicine, Hokkaido University, Sapporo, Japan
[6]Institute for the Advancement of Higher Education, Hokkaido University, Sapporo, Japan
[7]Division of Risk Analysis and Management, International Institute for Zoonosis Control, Hokkaido University, Sapporo, Japan
[8]Division of Molecular Virology and Genetics, Joint Research Center for Human Retrovirus Infection, Kumamoto University, Kumamoto, Japan
[9]Faculty of Medicine, Suez Canal University, Ismailia, Egypt
[10]Center for iPS Cell Research and Application (CiRA), Kyoto University, Kyoto, Japan
[11]First Medical Faculty at Biocev, Charles University, Vestec-Prague, Czechia
[12]Facultad de Ciencias de la Salud, Universidad Cardenal Herrera-CEU, CEU Universities, Valencia, Spain
[13]Department of Cancer Pathology, Faculty of Medicine, Hokkaido University, Sapporo, Japan
[14]Division of Systems Virology, Department of Microbiology and Immunology, The Institute of Medical Science, The University of Tokyo, Tokyo, Japan

(Affiliations continued on next page)

SUMMARY

In late 2023, several SARS-CoV-2 XBB descendants, notably EG.5.1, were predominant worldwide. However, a distinct SARS-CoV-2 lineage, the BA.2.86 variant, also emerged. BA.2.86 is phylogenetically distinct from other Omicron sublineages, accumulating over 30 amino acid mutations in its spike protein. Here, we examined the virological characteristics of the BA.2.86 variant. Our epidemic dynamics modeling suggested that the relative reproduction number of BA.2.86 is significantly higher than that of EG.5.1. Additionally, four clinically available antivirals were effective against BA.2.86. Although the fusogenicity of BA.2.86 spike is similar to that of the parental BA.2 spike, the intrinsic pathogenicity of BA.2.86 in hamsters was significantly lower than that of BA.2. Since the growth kinetics of BA.2.86 are significantly lower than those of BA.2 both *in vitro* and *in vivo*, the attenuated pathogenicity of BA.2.86 is likely due to its decreased replication capacity. These findings uncover the features of BA.2.86, providing insights for control and treatment.

INTRODUCTION

In November 2023, the SARS-CoV-2 XBB descendants, mainly EG.5.1 (originally XBB.1.9.2.5.1), are predominantly circulating worldwide according to Nextstrain (https://nextstrain.org/ncov/gisaid/global/6m). However, a lineage far distinct from XBB unexpectedly emerged and was named BA.2.86 on August 14, 2023.[1] Notably, BA.2.86 bears more than 30 mutations in the spike (S) protein compared with XBB and the parental BA.2, which are assumed to be associated with immune evasion.[2] Due to the higher number of amino acid substitutions in this variant, the World Health Organization (WHO) immediately designated BA.2.86 as a variant under monitoring on August 17, 2023.[3] As of December 2023, the BA.2.86 variant has been identified globally, with an increasing frequency in viral genome surveillance. Based on the epidemic situation, WHO designated BA.2.86 as a variant of interest on November 21, 2023.[3]

The immune evasive potential of BA.2.86 has been evaluated in recent studies, including ours.[2,4–9] Additionally, some studies addressed the virological features of BA.2.86, such as the affinity of the receptor-binding domain (RBD) of the BA.2.86 S to angiotensin-converting enzyme 2 (ACE2) receptor,[5,8] the fusogenicity of BA.2.86 S,[7] and the growth kinetics of a clinically isolated

Cell Host & Microbe
Short article

Mami Nagashima,[22] Kenji Sadamasu,[22] Kazuhisa Yoshimura,[22] The Genotype to Phenotype Japan (G2P-Japan) Consortium, Akatsuki Saito,[21,23,24] Jumpei Ito,[14,25] Takashi Irie,[26] Shinya Tanaka,[13,18,*] Jiri Zahradnik,[11,*] Terumasa Ikeda,[8,*] Kazuo Takayama,[10,27,*] Keita Matsuno,[2,3,7,28,*] Takasuke Fukuhara,[1,2,3,4,5,6,27,29,*] and Kei Sato[14,15,16,25,30,31,32,34,35,*]

[15]Graduate School of Medicine, The University of Tokyo, Tokyo, Japan
[16]Graduate School of Frontier Sciences, The University of Tokyo, Kashiwa, Japan
[17]Division of International Research Promotion, International Institute for Zoonosis Control, Hokkaido University, Sapporo, Japan
[18]Institute for Chemical Reaction Design and Discovery (WPI-ICReDD), Hokkaido University, Sapporo, Japan
[19]Indonesia International Institute for Life Sciences (i3L), Jakarta, Indonesia
[20]Faculty of Natural Science, Imperial College London, London, UK
[21]Department of Veterinary Science, Faculty of Agriculture, University of Miyazaki, Miyazaki, Japan
[22]Tokyo Metropolitan Institute of Public Health, Tokyo, Japan
[23]Center for Animal Disease Control, University of Miyazaki, Miyazaki, Japan
[24]Graduate School of Medicine and Veterinary Medicine, University of Miyazaki, Miyazaki, Japan
[25]International Vaccine Design Center, The Institute of Medical Science, The University of Tokyo, Tokyo, Japan
[26]Graduate School of Biomedical and Health Sciences, Hiroshima University, Hiroshima, Japan
[27]AMED-CREST, Japan Agency for Medical Research and Development, Tokyo, Japan
[28]International Collaboration Unit, International Institute for Zoonosis Control, Hokkaido University, Sapporo, Japan
[29]Laboratory of Virus Control, Research Institute for Microbial Diseases, Osaka University, Suita, Japan
[30]CREST, Japan Science and Technology Agency, Kawaguchi, Japan
[31]International Research Center for Infectious Diseases, The Institute of Medical Science, The University of Tokyo, Tokyo, Japan
[32]Collaboration Unit for Infection, Joint Research Center for Human Retrovirus Infection, Kumamoto University, Kumamoto, Japan
[33]These authors contributed equally
[34]X (formerly Twitter): @SystemsVirology
[35]Lead contact
*Correspondence: tanaka@med.hokudai.ac.jp (S.T.), jiri.zahradnik2@gmail.com (J.Z.), ikedat@kumamoto-u.ac.jp (T.I.), kazuo.takayama@cira.kyoto-u.ac.jp (K.T.), matsuk@czc.hokudai.ac.jp (K.M.), fukut@pop.med.hokudai.ac.jp (T.F.), keisato@g.ecc.u-tokyo.ac.jp (K.S.)
https://doi.org/10.1016/j.chom.2024.01.001

BA.2.86 in *in vitro* cell cultures.[7] However, other features of BA.2.86, such as the sensitivity to clinically available antiviral drugs and the intrinsic pathogenicity in hamsters, remain unknown. Here, we elucidated the virological features of SARS-CoV-2 BA.2.86 variant.

RESULTS AND DISCUSSION

Epidemic dynamics of BA.2.86

BA.2.86 is phylogenetically distinct from other Omicron sublineages that have emerged to date, exhibiting the accumulation of over 30 amino acid mutations in the S protein (Figures 1A and S1A). To assess the epidemic potential of BA.2.86, we estimated its relative effective reproduction number (R_e) (Figures 1B, 1C, and S1B; Table S1). Although we previously estimated the R_e of BA.2.86, that study did not conclusively determine whether BA.2.86 shows significantly higher R_e than EG.5.1, the currently dominant lineage globally.[2] This was mainly due to the considerable uncertainty on the estimated R_e of BA.2.86, attributed to a limited sequence dataset at that time. In our current analysis, we more accurately estimated the relative R_e of BA.2.86 by incorporating genome surveillance data from six countries where BA.2.86 is proliferating using a Bayesian hierarchical multinomial logistic model.[10,11] This method enabled us to estimate the R_e of each variant within individual countries (Figure S1B) as well as a global R_e average (Figure 1B). We show that the global average R_e of BA.2.86 is 1.07-fold higher than EG.5.1 (Figure 1B). Indeed, BA.2.86 is gradually growing in various countries, where EG.5.1 predominantly circulated (Figure 1C). Our data suggest that BA.2.86 will spread globally and become more prevalent.

Virological phenotype of BA.2.86 S

To investigate the virological features of BA.2.86 S, we measured the binding affinity of BA.2.86 S RBD to ACE2 receptor by the yeast display technique.[13] We have demonstrated that the XBB.1.5 S RBD exhibits the highest binding affinity to ACE2.[14] Notably, the ACE2 binding affinity of BA.2.86 S RBD was comparable to that of XBB.1.5 S RBD and significantly higher than those of the S RBDs of ancestral B.1.1, XBB.1, XBB.1.16, EG.5.1, and the parental BA.2 (Figure 2A).

To investigate the impact of hallmark mutations in the RBD of BA.2.86 S on the binding affinity to ACE2 receptor, we generated a set of reverse mutations based on BA.2.86 S RBD. As shown in Figure 2A, only a substitution, the K403R, significantly increased the dissociation constant (K_D) value when compared with the parental BA.2.86, suggesting that the R403K substitution can lead to increased ACE2 binding affinity. The decreased K_D values by the R403K substitution in the S RBDs of XBB.1, XBB.1.5, and BA.2 support the observation in BA.2.86 S RBD (Figure 2A). However, the K_D value of B.1.1 R403K was significantly larger than that of parental B.1.1 (Figure 2A), suggesting that the effect of R403K is epistatic and the increase of ACE2 binding affinity is observed only in the case of the backbone of BA.2-related S RBD.

We next performed an infection assay using HIV-1-based pseudovirus.[2] The assay showed that pseudoviruses with B.1.1 or EG.5.1 S showed significantly higher infectivity than that with BA.2 S, but pseudovirus with BA.2.86 S was comparable to that with BA.2 S (Figure 2B). To test the effect of each mutation on pseudovirus infectivity, we generated a total of 33 BA.2 derivatives that bear respective mutations in BA.2.86 (Figure 2B). Most of the mutations did not affect BA.2 S pseudovirus

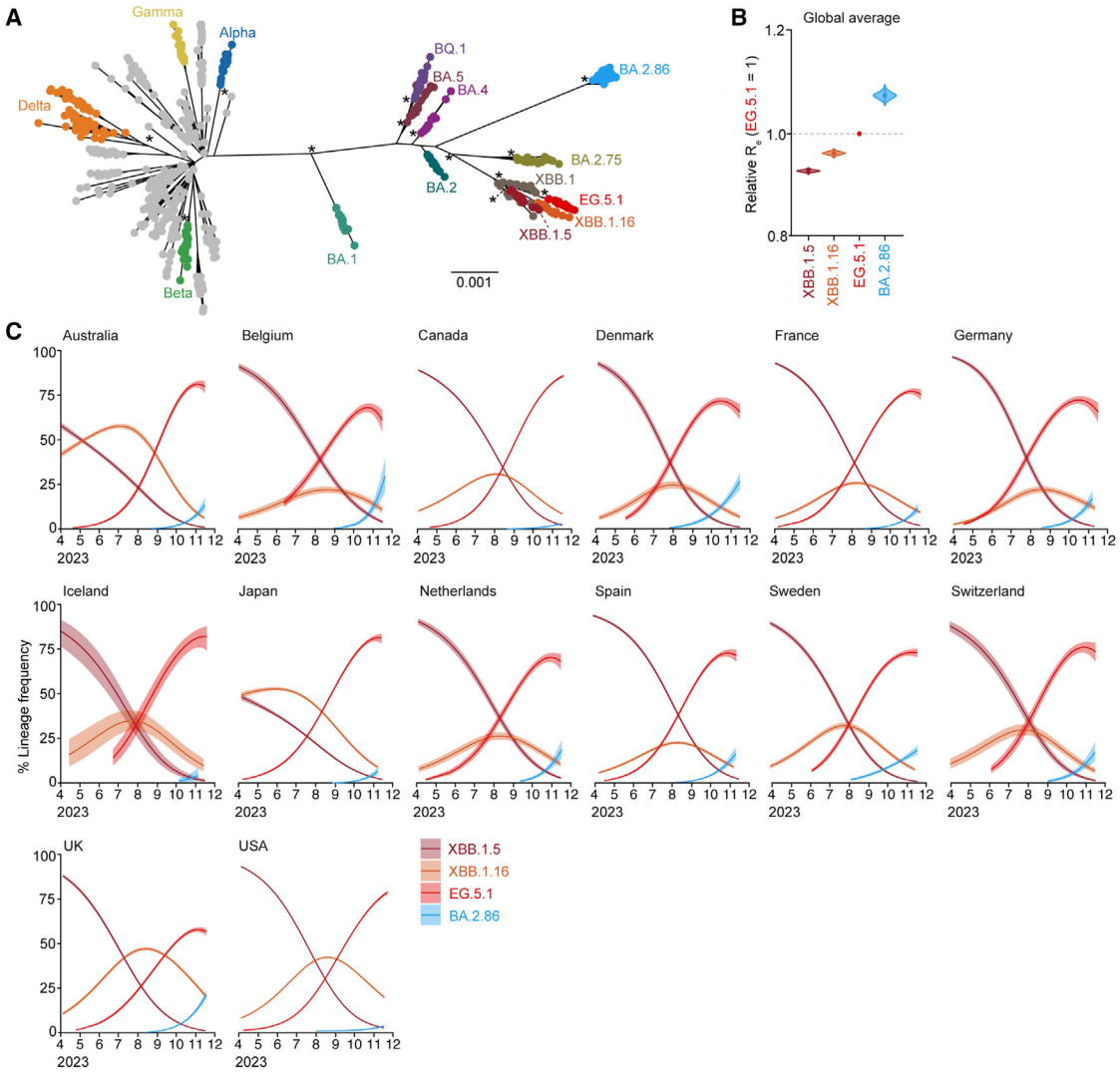

Figure 1. Virological features of the SARS-CoV-2 BA.2.86

(A) Maximum likelihood tree based on the complete genome of representative SARS-CoV-2 sequences. Twenty sequences were randomly sampled from each clade defined by Nextclade[12] and were included in the analysis. An asterisk represents a node with >0.95 bootstrap value. The scale bar represents genetic distance.

(B) Estimated relative R_e of each viral lineages, assuming a fixed generation time of 2.1 days. The relative R_e of EG.5.1 is designated to 1 (horizontal dashed line). The graph includes: the posterior distribution enclosed within the 99% Bayesian confidence interval (CI; violin), 95% CI (line), and posterior mean (dot). BA.2.86 and its sublineages, except for those with amino acid mutations in S (e.g., JN.1), are summarized as BA.2.86. The global average values estimated by a hierarchical Bayesian model[10] are presented. See also Figure S1B.

(C) Estimated lineage dynamics of BA.2.86 and the representative SARS-CoV-2 sublineages in fourteen countries where ≥100 BA.2.86 sequences were documented. The genome surveillance data from April 1, 2023 to November 15, 2023 were analyzed. The posterior mean is illustrated as the line, while the 95% Bayesian CI is shown as the ribbon.

See also Figure S1 and Table S1.

infectivity (Figure 2B). On the other hand, consistent with our previous reports,[11,14,15] certain mutations in the RBD, such as N460K and F486P, increased the pseudovirus infectivity (Figure 2B). Interestingly, three novel mutations in the N-terminal domain of the BA.2.86 S, F157S, N211del, and A264D, significantly increased the pseudovirus infectivity (Figure 2B). Our mutagenesis assay using pseudovirus suggested that while 6 out of the 33 mutations that are present in BA.2.86 but not in BA.2 increased the infectivity of BA.2, 16 out of the 33 mutations decreased the infectivity (Figure 2B). However, the overall infectivity of BA.2.86 was comparable to BA.2, suggesting that BA.2.86 might evolve its *S* gene probably to evade humoral immunity in hosts and then compensated for the decreased infectivity by obtaining infectivity-enhancing mutations (e.g., N460K and F486P, F157S, N211del, and A264D).

To examine the cleavage efficiency of S protein in the cells, the cells used for pseudovirus production were subjected to western blotting (Figures 2C and S2A–S2C). Interestingly, the

CellPress
OPEN ACCESS

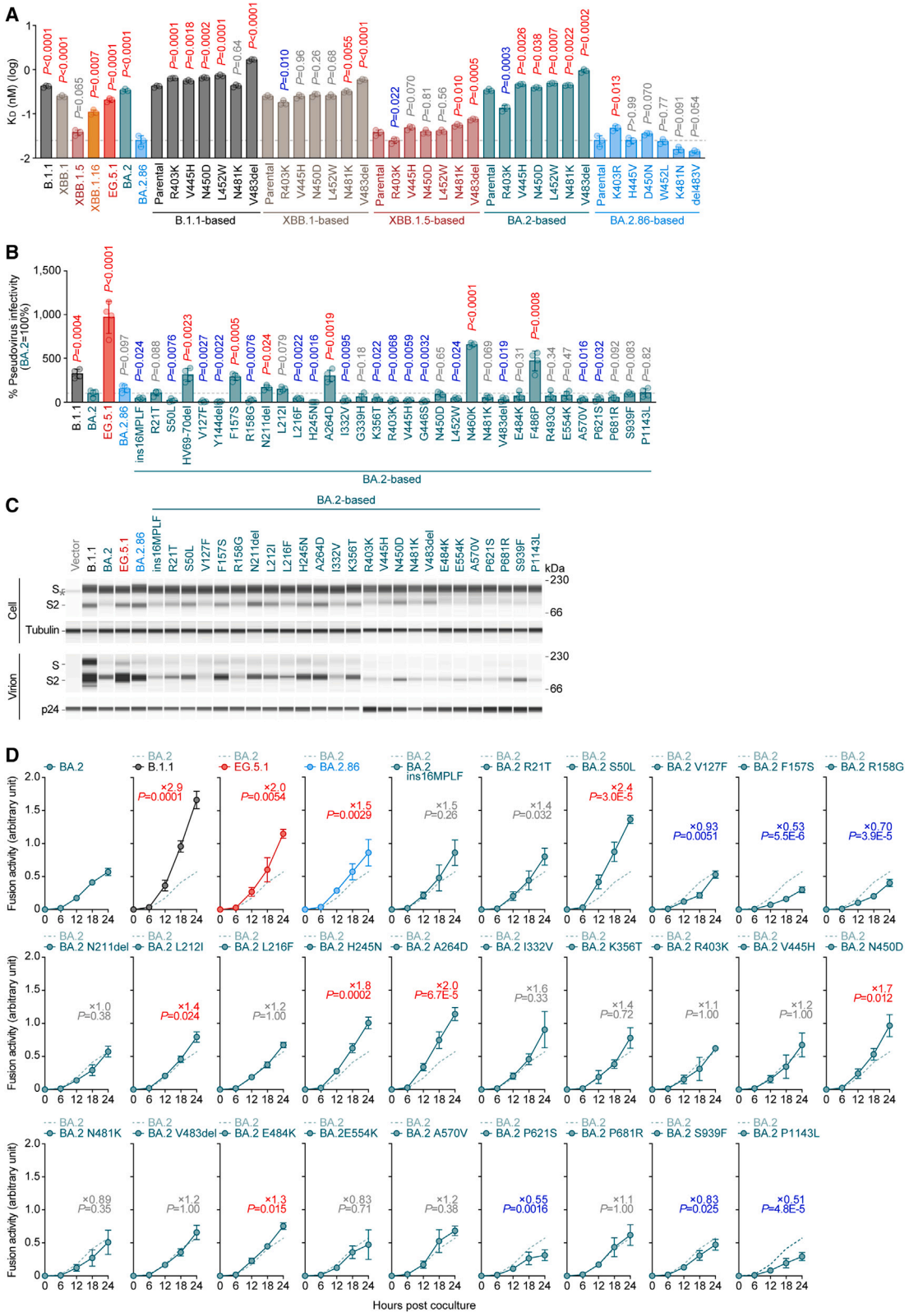

Figure 2. Virological phenotype of BA.2.86 S

(A) Binding affinity of the RBD of SARS-CoV-2 S proteins to ACE2 by yeast surface display. The dissociation constant (K_D) value indicating the binding affinity of SARS-CoV-2 S RBD to soluble ACE2 when expressed on yeast is shown. Each dot indicates the result of an individual replicate. The dashed horizontal lines

(legend continued on next page)

band intensity of S2 in the cells expressing BA.2.86 S was higher than that of the cells expressing BA.2 S. The results from respective point mutants based on BA.2 S showed that several mutations contributed to increased efficiency of S cleavage. In addition to the S cleavage efficacy in the cells, the level of S2 in the virions pseudotyped with BA.2.86 S was higher than that with BA.2 S. While the levels of virion-incorporated S2 protein of respective BA.2-based point mutants were different from each other, three mutants (F157S, A264D, and N460K) with increased cleavage efficacy in the cells exhibited increased incorporation of S2 proteins in the released viral particles (Figures 2C, S2A, and S2B).

Fusogenicity of BA.2.86 S

We then investigated the fusogenicity of BA.2.86 S protein by the S-protein-mediated membrane fusion assay (Figure S2D).[16] The surface expression level of BA.2.86 S was comparable to that of the parental BA.2 S (Figure S2E). Several mutations in BA.2.86 significantly increased the expression level of BA.2 S on the cell surface (Figure S2E).

Consistent with previous reports,[10,17,18] B.1.1, XBB.1.5, and EG.5.1 S proteins were significantly more fusogenic than BA.2 S protein (Figures 2D and S2F). Notably, the fusogenicity of BA.2.86 S was significantly greater than that of BA.2 S (Figures 2D and S2F). This prompted us to determine the amino acid residues responsible for the increased fusogenicity. We found that four substitutions in the N-terminal domain (S50L, L212I, H245N, and A264D), and two substitutions in the RBD (N450D and E484K) significantly increased the S-mediated fusogenicity (Figures 2D and S2F). Interestingly, we have demonstrated that the P681R substitution, a hallmark mutation in the Delta variant, significantly increased the fusogenicity of ancestral B.1.1-based S.[19] However, the P681R substitution did not affect the fusogenicity of BA.2 S (Figures 2D and S2F). Similar to the effect of R403K substitution on ACE2 binding by yeast surface display (Figure 2A), our results suggest that the effect of certain substitutions (e.g., R403K and P681R) on the virological feature of SARS-CoV-2 S is epistatic.

Immune evasion of BA.2.86

We have recently reported that BA.2.86 is more resistant to XBB breakthrough infection (BTI) sera than EG.5.1.[2] To evaluate the sensitivity of BA.2.86 to antiviral humoral immunity elicited by the BTI with other Omicron sublineages, we performed neutralization assays using BA.2 BTI sera (n = 13) and BA.5 BTI sera (n = 17). As shown in Figure S2G, the 50% neutralization titer (NT_{50}) of BA.2 BTI sera against BA.2.86 was significantly (43-fold) lower than those against the B.1.1 ($p < 0.0001$) as well as EG.5.1. A similar trend was observed in the BA.5 BTI sera (20-fold, $p < 0.0001$) (Figure S2H). These results suggest that BA.2.86 has a potent immune evasion ability from humoral immunity induced by BA.2/BA.5 BTI. It would be valuable to experimentally address the potentially critical sites that may be responsible for this evasion. However, as mentioned above, there are 33 mutations in the BA.2.86 S when compared with the parental BA.2, and substantial additional investigation would therefore be required.

In the case of BA.2 BTI, the NT_{50} values of BA.2.86 were comparable to that of EG.5.1 (Figure S2G). Interestingly, however, the NT_{50} of BA.5 BTI sera against BA.2.86 showed a higher value than EG.5.1 ($p = 0.02$; Figure S2H), suggesting that BA.2.86 is more sensitive to BA.5 BTI sera than EG.5.1.

Growth kinetics of clinically isolated BA.2.86 *in vitro*

To investigate the growth kinetics of BA.2.86 *in vitro*, clinical isolates of BA.2.86, EG.5.1, and BA.2 were inoculated into VeroE6/TMPRSS2 (Figure 3A), Vero cells (Figure 3C), airway organoids-derived air-liquid interface (AO-ALI) model (Figure 3D), Calu-3 cells (Figure 3E), and colon organoids (Figure 3F). In VeroE6/TMPRSS2 cells, the growth kinetics of BA.2.86 and BA.2 were comparable, while BA.2.86 was less replicative than EG.5.1 (Figure 3A). An immunofluorescence assay at 72 h post infection (h.p.i.) further showed that VeroE6/TMPRSS2 cells infected with BA.2.86 exhibited lower GFP intensity than EG.5.1-infected cells (Figure 3B). On the other hand, in Vero cells, AO-ALI, and Calu-3 cells, the replication efficiency of BA.2.86 was significantly lower than that of EG.5.1 and BA.2 (Figures 3C–3E). These results suggest that BA.2.86 showed a poorer replication capacity compared with EG.5.1 and BA.2. However, in colon organoids, the replication efficiency of BA.2.86 was similar to that of EG.5.1 and BA.2 (Figure 3F) suggesting that the viral replication capacity of BA.2.86 in respiratory cells is different from that in intestinal cells.

Examining the impact of BA.2.86 infection on the airway epithelial-endothelial barrier

To investigate the consequences of BA.2.86 infection on the airway epithelial and endothelial barriers, we utilized an airway-on-a-chip system.[20] The volume of viruses penetrating from

indicate the value of BA.2. Statistically significant differences versus each parental S protein and those between BA.2 were determined by two-sided students' t tests.

(B) Pseudovirus assay. HOS-ACE2/TMPRSS2 cells were infected with pseudoviruses bearing each S. The amount of input virus was normalized based on the amount of HIV-1 p24 capsid protein. The percent infectivity compared with that of the virus pseudotyped with the BA.2 S are shown. Assays were performed in quadruplicate. The presented data are expressed as the average ± SD. Each dot indicates the result of an individual replicate. The dashed horizontal lines indicate the value of BA.2. Statistically significant differences versus each parental S protein and those between BA.2 were determined by two-sided students' t tests.

(C) Western blotting of S protein in cells and virions. Representative blots of S-expressing cells ("cell") and supernatants ("virion") of four independent experiments are shown. The gray asterisk indicates the background/non-specific signal. Tubulin and HIV-1 p24 were used for the internal controls of cell and virion, respectively. kDa, kilodalton.

(D) S-based fusion assay in Calu-3 cells. The recorded fusion activity is shown. The dashed green line indicates the result of BA.2. The red number in each panel indicates the fold difference between BA.2 and the derivative tested at 24 h post coculture. Assays were performed in quadruplicate. Statistically significant differences versus BA.2 across time points were determined by multiple regression. The familywise error rates (FWERs) calculated using the Holm method are indicated in the figures.

See also Figure S2.

CellPress
OPEN ACCESS

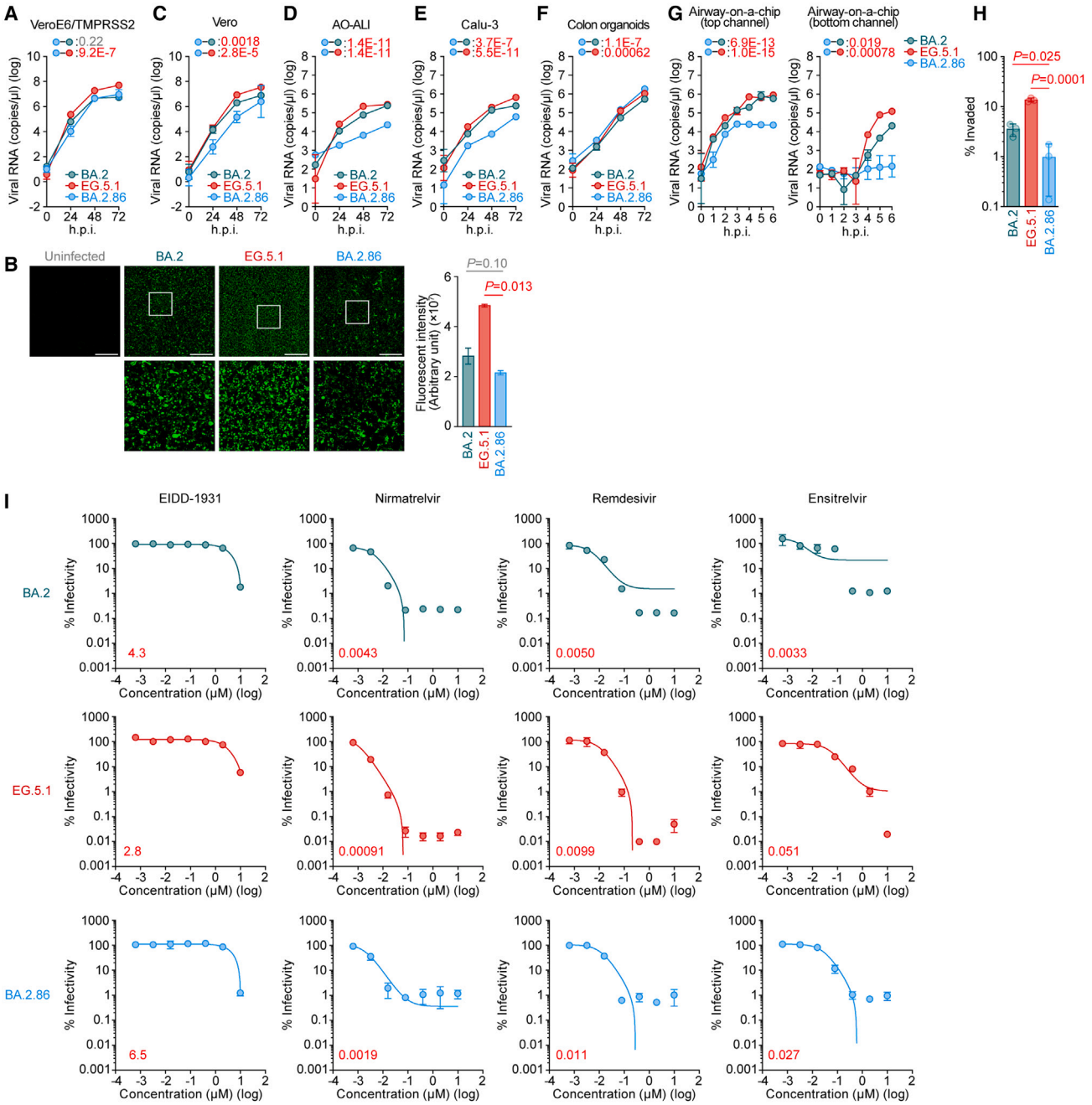

Figure 3. Growth kinetics of BA.2.86 and the antiviral effect of clinically available compounds against BA.2.86

(A and C–F) Growth kinetics of BA.2.86 in cell cultures. Clinical isolates of BA.2.86, EG.5.1, and BA.2 were inoculated into VeroE6/TMPRSS2 cells (A), Vero cells (C), AO-ALI (D), Calu-3 cells (E), and colon organoids (F). The copy numbers of viral RNA in the culture supernatant were routinely quantified by quantitative reverse-transcription PCR (RT-qPCR).

(B) Immunofluorescence staining. Infected VeroE6/TMPRSS2 cells (multiplicity of infection [MOI]) = 0.01) at 72 h.p.i. were stained with anti-SARS-CoV-2 N antibody. Higher-magnification views of the regions indicated by squares are shown. Scale bars, 1,000 μm. Left, representative panels. Higher-magnification views of the regions indicated by squares are shown at the bottom. Right, the GFP intensity of the stained cells was measured.

(G and H) Clinical isolates of BA.2, EG.5.1, and BA.2.86 were inoculated into an airway-on-a-chip system. The copy numbers of viral RNA in the top and bottom channels of an airway-on-a-chip were routinely quantified by RT-qPCR (G). The percentage of viral RNA load in the bottom channel per top channel at 6 d.p.i. (i.e., % invaded virus from the top channel to the bottom channel) is shown (H).

(I) Effect of antiviral drugs against BA.2.86. Antiviral effects of the four drugs (EIDD-1931, nirmatrelvir [also known as PF-07321332], remdesivir, and ensitrelvir) in human iPSC-derived lung organoids. The assay of each antiviral drugs was performed in triplicate, and the 50% effective concentration (EC_{50}) was calculated.

the upper channel to the lower channel serves as an indicator of the viruses' ability to breach the airway epithelial and endothelial barriers. Significantly, the proportion of viruses that penetrated the lower channel of the BA.2.86-infected airway-on-a-chip was lower compared with BA.2- and EG.5.1-infected airway-on-a-chip (Figures 3G and 3H).

Antiviral effect of clinically available compounds against BA.2.86

We evaluated the sensitivity of BA.2.86 to four antiviral drugs, EIDD-1931, nirmatrelvir (also known as PF-07321332), remdesivir, and ensitrelvir. Clinical isolates of BA.2 and EG.5.1 were used as controls. The viruses were inoculated into human induced pluripotent stem cell (iPSC)-derived lung organoids, a physiologically relevant model, and treated with the four antiviral drugs. Nirmatrelvir showed the strongest antiviral effects, and no differences in antiviral efficacy were observed between the three variants (Figure 3I). Remdesivir and ensitrelvir showed significant antiviral effects on the three isolates, while EIDD-1931 showed moderate antiviral effects on the three isolates (Figure 3I).

Intrinsic pathogenicity of clinically isolated BA.2.86 *in vivo*

To investigate the virological features of BA.2.86 *in vivo*, clinical isolates of BA.2.86, EG.5.1, and BA.2 (2,000 50% tissue culture infectious dose [$TCID_{50}$]) were intranasally inoculated into hamsters under anesthesia. All infected hamsters exhibited the loss of body weight (Figure 4A). However, the loss of body weight of BA.2.86-infected hamsters was significantly less than those of the hamsters infected with EG.5.1 and BA.2 (Figure 4A).

We then analyzed the pulmonary function of infected hamsters as reflected by two parameters, enhanced pause (Penh) and the ratio of time to peak expiratory flow relative to the total expiratory time (Rpef). Infection of EG.5.1 and BA.2 resulted in significant differences in these two respiratory parameters at 3 days postinfection (d.p.i.) (Figure 4A). On the other hand, these two parameters of BA.2.86-infected hamsters were constant (Figure 4A). These results suggest that BA.2.86 is less pathogenic in hamsters than EG.5.1 and BA.2.

To evaluate viral spread in infected hamsters, we routinely measured the viral RNA load in oral swabs and the two lung regions, lung hilum and periphery. The viral RNA load of the hamsters infected with EG.5.1 and BA.2 were comparable (Figure 4B). On the other hand, the viral RNA load of BA.2.86-infected hamsters was significantly lower than those of EG.5.1- and BA.2-infected hamsters (Figure 4B), suggesting that the replication efficacy of BA.2.86 *in vivo* is lower than that of EG.5.1 and BA.2.

To further investigate the differences of viral spreading in the respiratory tissues of the infected hamsters, formalin-fixed right lungs of infected hamsters were analyzed at 2 and 5 d.p.i. We carefully identified the four lobules and lobar bronchi sectioning each lobe along with the bronchial branches, and performed immunohistochemical (IHC) analysis targeting the viral nucleocapsid (N) protein as performed in our previous studies.[10,11,15,19,21–23] The percentage of N-positive cells in the lungs of BA.2.86-infected hamsters was significantly lower than that of BA.2- and EG.5.1-infected hamsters (Figures 4C and S3A). At 5 d.p.i., N-positive cells were slightly detected in the peripheral alveolar space of any Omicron-variant-infected hamsters, and N-positive area of BA.2.86-infected hamsters tended to be lower than that of BA.2 and EG.5.1-infected hamsters (Figures 4C and S3B).

To evaluate the intrinsic pathogenicity of BA.2.86, histopathological scoring was performed according to the criteria described in our previous studies.[19] In BA.2.86-infected hamsters, bronchitis/bronchiolitis was milder than in the BA.2- and the EG.5.1-infected hamsters, and inflammation area including alveolar damage and type II pneumocytes were smaller at 2 d.p.i. (Figures 4D and S4A). Histopathological scores including bronchitis/bronchiolitis, hemorrhage/congestion, alveolar damage, and area of type II pneumocytes were lower than those of BA.2 and EG.5.1 at 5 d.p.i. (Figures 4D and S4B). Among the Omicron subvariants we examined in this study, the total histopathological score of BA.2.86-infeted hamsters was lowest at 2 and 5 d.p.i. (Figure 4E).

In summary, here, we elucidated the virological characteristics of BA.2.86. In our previous investigations, we observed that the S cleavage efficacy, fusogenicity, and intrinsic pathogenicity in hamsters were well correlated with each other.[10,19,21,22] For instance, the Delta S is efficiently cleaved by furin and is highly fusogenic, and the Delta isolate is more pathogenic than ancestral SARS-CoV-2 variants.[19] In sharp contrast, the Omicron BA.1 S is faintly cleaved by furin and poorly fusogenic, and the BA.1 isolate is less pathogenic than ancestral SARS-CoV-2.[21] Here, we showed that BA.2.86 S is more efficiently cleaved than BA.2 S, but the fusogenicity of BA.2.86 S and BA.2 S is similar. Notably, although the fusogenicity of the S proteins of BA.2.86 and BA.2 were comparable, the intrinsic pathogenicity of BA.2.86 in hamsters was significantly lower than that of BA.2. This discrepancy can be explained by the lower replication capacity of BA.2.86. In fact, we showed that the replication kinetics of BA.2.86 is significantly less efficient than that of BA.2 in *in vitro* cell culture and *in vivo*. Therefore, our results suggest that the attenuated pathogenicity of BA.2.86 is attributed to its decreased replication capacity.

The BA.2.86 lineage, including the latest sublineage JN.1, is rapidly expanding worldwide as of January 2024. We should carefully monitor this lineage having the potential to be the next predominant lineage by replacing the current XBB lineage.

CONSORTIA

The members of The Genotype to Phenotype Japan (G2P-Japan) Consortium are Yu Kaku, Naoko Misawa, Arnon Plianchaisuk, Kaoru Usui, Wilaiporn Saikruang, Shigeru Fujita, Luo Chen, Lin Pan, Mai Suganami, Mika Chiba, Ryo Yoshimura, Kyoko Yasuda, Keiko Iida, Adam Patrick Strange, Naomi Ohsumi, Shiho Tanaka, Kaho Okumura, Hirofumi Sawa, Jingshu Li, Tomoya Tsubo, Zannatul Ferdous, Kenji Shishido, Saori Suzuki, Hayato Ito, Isao Yoshida, So Nakagawa, Kotaro Shirakawa, Akifumi Takaori-Kondo, Kayoko Nagata, Ryosuke Nomura, Yoshihito Horisawa, Yusuke Tashiro, Yugo Kawai, Rina Hashimoto, Yukio Watanabe, Yoshitaka Nakata, Hiroki Futatsusako, Ayaka Sakamoto, Naoko Yasuhara, Takao Hashiguchi, Tateki Suzuki, Kanako Terakado Kimura, Jiei Sasaki, Yukari Nakajima, Hisano Yajima, Ryoko Kawabata, Kaori Sasaki-Tabata, MST Monira Begum, Yuka Mugita, Sharee Leong, Otowa Takahashi, Kimiko Ichihara, Takamasa Ueno, Chihiro Motozono, Mako Toyoda, Maya Shofa, Yuki

CellPress
OPEN ACCESS

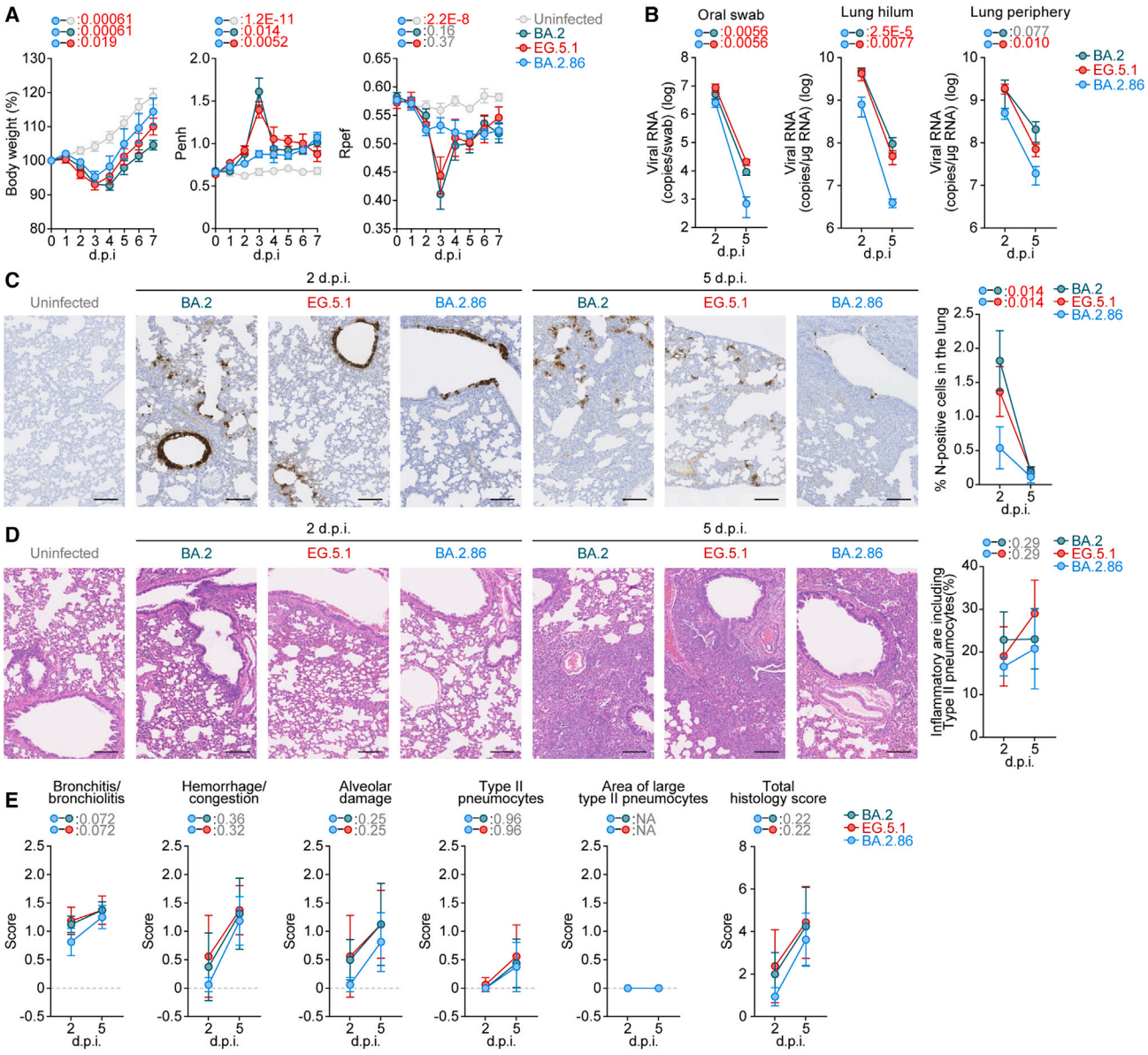

Figure 4. Virological features of BA.2.86 *in vivo*

Syrian hamsters were intranasally inoculated with BA.2.86, EG.5.1, and BA.2. Six hamsters of the same age were intranasally inoculated with saline (uninfected).

(A) Time-course analysis. Six hamsters per group were used to routinely measure body weight (left), Penh (middle), and Rpef (right).

(B) Viral RNA load. Four hamsters per group were euthanized at 2 and 5 d.p.i. and quantified viral RNA load in oral swab (left), lung hilum (middle), and lung periphery (B, right) by RT-qPCR.

(C) IHC of the viral N-protein in the lungs at 2 (left) and 5 d.p.i. (right) of infected hamsters. Representative figures are shown. N-positive cells are shown in brown.

(D) H&E staining of the lungs of infected hamsters. Representative figures are shown. Uninfected lung alveolar space is also shown.

(E) Histopathological scoring of lung lesions (n = 4 per infection group). Representative pathological features are reported in our previous studies.[10,11,15,19,21–23]

In (A)–(C) and (E), data are presented as the average ± SEM. In (A), the 0 d.p.i. data were excluded from the analyses. The FWERs calculated using the Holm method are indicated in the figures.

In (A) and (B), statistically significant differences between BA.2.86 and other variants across time points were determined by multiple regression.

In (A), (B), and (E), statistically significant differences between BA.2.86 and other variants across time points were determined by multiple regression. In (B) and (E), the 0 d.p.i. data were excluded from the analyses. The FWERs calculated using the Holm method are indicated in the figures.

In (C), each dot indicates the result of an individual hamster. Statistically significant differences between BA.2.86 and other variants were determined by a two-sided Mann-Whitney U test.

In (C) and (D), each panel shows a representative result from an individual infected hamster. Scale bars, 200 μm in (C) and (D).

See also Figures S3 and S4.

Shibatani, Tomoko Nishiuchi, Prokopios Andrikopoulos, and Aditi Konar.

STAR★METHODS

Detailed methods are provided in the online version of this paper and include the following:

- KEY RESOURCES TABLE
- RESOURCE AVAILABILITY
  - Lead contact
  - Materials availability
  - Data and code availability
- EXPERIMENTAL MODEL AND SUBJECT DETAILS
  - Ethics statement
  - Human serum collection
  - Cell culture
  - Human lung organoids
  - Animal experiments
- METHOD DETAILS
  - Phylogenetic analysis
  - Epidemic dynamics analysis
  - Viral genome sequencing
  - Plasmid construction
  - Yeast surface display analysis
  - Pseudovirus infection
  - Western blotting
  - SARS-CoV-2 S-based fusion assay
  - SARS-CoV-2 preparation and titration
  - SARS-CoV-2 infection
  - Immunofluorescence staining
  - RT–qPCR
  - Airway-on-a-chip
  - Microfluidic device
  - Antiviral drug assay using SARS-CoV-2 clinical isolates and human iPSC-derived lung organoids
  - Lung function test
  - Immunohistochemistry
  - H&E staining
  - Histopathological scoring
- QUANTIFICATION AND STATISTICAL ANALYSIS

SUPPLEMENTAL INFORMATION

Supplemental information can be found online at https://doi.org/10.1016/j.chom.2024.01.001.

ACKNOWLEDGMENTS

We would like to thank all members belonging to The Genotype to Phenotype Japan (G2P-Japan) Consortium. We gratefully acknowledge all data contributors, i.e., the authors and their originating laboratories responsible for obtaining the specimens, and their submitting laboratories for generating the genetic sequence and metadata and sharing via the GISAID Initiative, on which this research is based. The super-computing resource was provided by Human Genome Center at The University of Tokyo. This study was supported in part by AMED SCARDA Japan Initiative for World-leading Vaccine Research and Development Centers "UTOPIA" (JP223fa627001, to K. Sato), AMED SCARDA Program on R&D of new generation vaccine including new modality application (JP223fa727002, to K. Sato); AMED Research Program on Emerging and Re-emerging Infectious Diseases (JP22fk0108617 to T.F.; JP22fk0108146, to K. Sato; JP22fk0108534, to T. Irie, T. Ikeda, and K. Sato; JP22fk0108511, to A.S., T. Ikeda, Keita Matsuno, S. Tanaka, K.T., T.F., and K. Sato; JP22fk0108506, to A.S., K.T., and K. Sato); AMED Japan Program for Infectious Diseases Research and Infrastructure (JP22wm0125008 to Keita Matsuno); AMED-CREST (JP21gm1610005, to K.T.; JP22gm1610008, to T.F.); JST PRESTO (JPMJPR22R1, to J.I.); JST CREST (JPMJCR20H4, to K. Sato); JSPS KAKENHI Fund for the Promotion of Joint International Research (International Leading Research) (JP23K20041, to A.S., Keita Matsuno, T.F., and K. Sato); JSPS Grant-in-Aid for Scientific Research C (22K07103, to T. Ikeda); JSPS KAKENHI Grant-in-Aid for Scientific Research B (21H02736, to T.F.); JSPS KAKENHI Grant-in-Aid for Early-Career Scientists (22K16375, to H.N.; 20K15767, J.I.); JSPS Core-to-Core Program (A. Advanced Research Networks) (JPJSCCA20190008, to K. Sato); JSPS Research Fellow (DC2 22J11578, to K.U.; DC1 23KJ0710, to Y. Kosugi); JSPS Leading Initiative for Excellent Young Researchers (to T. Ikeda); World-leading Innovative and Smart Education (WISE) Program 1801 from the Ministry of Education, Culture, Sports, Science and Technology (MEXT) (to N.N.); Ministry of Health, Labour and Welfare 23HA2010 (to N.N. and Keita Matsuno); The Cooperative Research Program of Institute for Life and Medical Sciences, Kyoto University (to K. Sato); International Joint Research Project of the Institute of Medical Science, the University of Tokyo (to A.S., T. Ikeda, J.Z., and T.F.); Takeda Science Foundation (to T. Ikeda and T.F.); Mochida Memorial Foundation for Medical and Pharmaceutical Research (to T. Ikeda); The Naito Foundation (to T. Ikeda); Mitsubishi Foundation (to K. Sato); Hirose Foundation (to T.T.); Japanese Government MEXT Scholarship-Research Category (220235 to J.E.M.T.) and the project of National Institute of Virology and Bacteriology, Programme EXCELES, funded by the European Union, Next Generation EU (LX22NPO5103, to J.Z.). We express our gratitude to CEU Universities and Santander Bank (Ayudas a la movilidad internacional de los investigadores en formación de la CEINDO) and the Federation of European Biochemical Societies (FEBS; Short-Term Fellowship), for their financial support to M.P.-B.

AUTHOR CONTRIBUTIONS

H.N., S.D., K.U., R.S., M.J., Y. Kosugi, Z.G., A.A.H., O.P., Y. Kim, Y.L.T., and T. Irie performed cell culture experiments. T.T., Keita Mizuma, S. Tsujino, R.S., I.K., N.N., Keita Matsuno, and T.F. performed animal experiments. Y.O., L.W., M.T., and S. Tanaka performed histopathological analysis. M.P.-B. and J.Z. performed yeast surface display assay. S.D. and K.T. prepared human iPSC-derived lung organoids, AO-ALI, and airway-on-a-chip systems. S.D. and K.T. performed antiviral drug tests. J.E.M.T. performed bioinformatics analyses. J.I. designed bioinformatics analyses and interpreted the results. A.S., J.I., T. Irie, S. Tanaka, J.Z., T. Ikeda, K.T., Keita Matsuno, T.F., and K. Sato designed the experiments and interpreted the results. J.I., S. Tanaka, J.Z., T. Ikeda, K.T., Keita Matsuno, T.F., and K. Sato wrote the original manuscript. All authors reviewed and proofread the manuscript. The Genotype to Phenotype Japan (G2P-Japan) Consortium contributed to the project administration.

DECLARATION OF INTERESTS

J.I. has consulting fees and honoraria for lectures from Takeda Pharmaceutical Co. Ltd. K. Sato has consulting fees from Moderna Japan Co., Ltd. and Takeda Pharmaceutical Co. Ltd. and honoraria for lectures from Gilead Sciences, Inc., Moderna Japan Co., Ltd., and Shionogi & Co., Ltd.

Received: November 2, 2023
Revised: December 5, 2023
Accepted: January 4, 2024
Published: January 26, 2024

REFERENCES

1. GitHub (2023). 2nd-Generation BA.2 Saltation Lineage, >30 spike mutations (3 seq, 2 countries, Aug 14) (GitHub). https://github.com/cov-lineages/pango-designation/issues/2183#issue-1849123156.
2. Uriu, K., Ito, J., Kosugi, Y., Tanaka, Y.L., Mugita, Y., Guo, Z., Hinay, A.A., Putri, O., Kim, Y., Shimizu, R., et al. (2023). Transmissibility, infectivity, and

immune evasion of the SARS-CoV-2 BA.2.86 variant. Lancet Infect. Dis. *23*, e460–e461.

3. WHO (2023). Tracking SARS-CoV-2 variants. https://www.who.int/en/activities/tracking-SARS-CoV-2-variants.
4. Lasrado, N., Collier, A.Y., Hachmann, N.P., Miller, J., Rowe, M., Schonberg, E.D., Rodrigues, S.L., LaPiana, A., Patio, R.C., Anand, T., et al. (2023). Neutralization escape by SARS-CoV-2 Omicron subvariant BA.2.86. Vaccine *41*, 6904–6909.
5. Wang, Q., Guo, Y., Liu, L., Schwanz, L.T., Li, Z., Nair, M.S., Ho, J., Zhang, R.M., Iketani, S., Yu, J., et al. (2023). Antigenicity and receptor affinity of SARS-CoV-2 BA.2.86 spike. Nature *624*, 639–644.
6. Sheward, D.J., Yang, Y., Westerberg, M., Öling, S., Muschiol, S., Sato, K., Peacock, T.P., Karlsson Hedestam, G.B., Albert, J., and Murrell, B. (2023). Sensitivity of the SARS-CoV-2 BA.2.86 variant to prevailing neutralising antibody responses. Lancet Infect. Dis. *23*, e462–e463.
7. Qu, P., Xu, K., Faraone, J.N., Goodarzi, N., Zheng, Y.-M., Carlin, C., Bednash, J.S., Horowitz, J.C., Mallampalli, R.K., Saif, L.J., et al. (2023). Immune Evasion, Infectivity, and Fusogenicity of SARS-CoV-2 Omicron BA.2.86 and FLip Variants. Preprint at bioRxiv.
8. Yang, S., Yu, Y., Jian, F., Song, W., Yisimayi, A., Chen, X., Xu, Y., Wang, P., Wang, J., Yu, L., et al. (2023). Antigenicity and infectivity characterisation of SARS-CoV-2 BA.2.86. Lancet Infect. Dis. *23*, e457–e459.
9. Khan, K., Lustig, G., Römer, C., Reedoy, K., Jule, Z., Karim, F., Ganga, Y., Bernstein, M., Baig, Z., Jackson, L., et al. (2023). Evolution and neutralization escape of the SARS-CoV-2 BA.2.86 subvariant. Nat. Commun. *14*, 8078.
10. Yamasoba, D., Kimura, I., Nasser, H., Morioka, Y., Nao, N., Ito, J., Uriu, K., Tsuda, M., Zahradnik, J., Shirakawa, K., et al. (2022). Virological characteristics of the SARS-CoV-2 Omicron BA.2 spike. Cell *185*, 2103–2115.e19.
11. Saito, A., Tamura, T., Zahradnik, J., Deguchi, S., Tabata, K., Anraku, Y., Kimura, I., Ito, J., Yamasoba, D., Nasser, H., et al. (2022). Virological characteristics of the SARS-CoV-2 Omicron BA.2.75 variant. Cell Host Microbe *30*, 1540–1555.e15.
12. Hadfield, J., Megill, C., Bell, S.M., Huddleston, J., Potter, B., Callender, C., Sagulenko, P., Bedford, T., and Neher, R.A. (2018). Nextstrain: real-time tracking of pathogen evolution. Bioinformatics *34*, 4121–4123.
13. Zahradník, J., Marciano, S., Shemesh, M., Zoler, E., Harari, D., Chiaravalli, J., Meyer, B., Rudich, Y., Li, C., Marton, I., et al. (2021). SARS-CoV-2 variant prediction and antiviral drug design are enabled by RBD in vitro evolution. Nat. Microbiol. *6*, 1188–1198.
14. Uriu, K., Ito, J., Zahradnik, J., Fujita, S., Kosugi, Y., Schreiber, G.; Genotype to Phenotype Japan (G2P-Japan) Consortium, and Sato, K. (2023). Enhanced transmissibility, infectivity, and immune resistance of the SARS-CoV-2 omicron XBB.1.5 variant. Lancet Infect. Dis. *23*, 280–281.
15. Ito, J., Suzuki, R., Uriu, K., Itakura, Y., Zahradnik, J., Kimura, K.T., Deguchi, S., Wang, L., Lytras, S., Tamura, T., et al. (2023). Convergent evolution of SARS-CoV-2 Omicron subvariants leading to the emergence of BQ.1.1 variant. Nat. Commun. *14*, 2671.
16. Ikeda, T., Begum, M.M.S.T., Ichihara, K., Takahashi, O., Nasser, H., Jonathan, M., Tokunaga, K., Yoshida, I., Nagashima, M., Sadamasu, K., et al. (2023). Virological characteristics correlating with SARS-CoV-2 spike protein fusogenicity. Preprint at bioRxiv.
17. Tamura, T., Irie, T., Deguchi, S., Yajima, H., Tsuda, M., Nasser, H., Mizuma, K., Plianchaisuk, A., Suzuki, S., Uriu, K., et al. (2023). Virological characteristics of the SARS-CoV-2 XBB.1.5 variant. Preprint at bioRxiv.
18. Tsujino, S., Deguchi, S., Nomai, T., Padilla-Blanco, M., Plianchaisuk, A., Wang, L., Begum, M.M.S.T., Uriu, K., Mizuma, K., Nao, N., et al. (2023). Virological characteristics of the SARS-CoV-2 Omicron EG.5.1 variant. Preprint at bioRxiv.
19. Saito, A., Irie, T., Suzuki, R., Maemura, T., Nasser, H., Uriu, K., Kosugi, Y., Shirakawa, K., Sadamasu, K., Kimura, I., et al. (2022). Enhanced fusogenicity and pathogenicity of SARS-CoV-2 Delta P681R mutation. Nature *602*, 300–306.
20. Hashimoto, R., Takahashi, J., Shirakura, K., Funatsu, R., Kosugi, K., Deguchi, S., Yamamoto, M., Tsunoda, Y., Morita, M., Muraoka, K., et al. (2022). SARS-CoV-2 disrupts the respiratory vascular barrier by suppressing Claudin-5 expression. Sci. Adv. *8*, eabo6783.
21. Suzuki, R., Yamasoba, D., Kimura, I., Wang, L., Kishimoto, M., Ito, J., Morioka, Y., Nao, N., Nasser, H., Uriu, K., et al. (2022). Attenuated fusogenicity and pathogenicity of SARS-CoV-2 Omicron variant. Nature *603*, 700–705.
22. Kimura, I., Yamasoba, D., Tamura, T., Nao, N., Suzuki, T., Oda, Y., Mitoma, S., Ito, J., Nasser, H., Zahradnik, J., et al. (2022). Virological characteristics of the novel SARS-CoV-2 Omicron variants including BA.4 and BA.5. Cell *185*, 3992–4007.e16.
23. Tamura, T., Ito, J., Uriu, K., Zahradnik, J., Kida, I., Anraku, Y., Nasser, H., Shofa, M., Oda, Y., Lytras, S., et al. (2023). Virological characteristics of the SARS-CoV-2 XBB variant derived from recombination of two Omicron subvariants. Nat. Commun. *14*, 2800.
24. Tamura, T., Yamasoba, D., Oda, Y., Ito, J., Kamasaki, T., Nao, N., Hashimoto, R., Fujioka, Y., Suzuki, R., Wang, L., et al. (2023). Comparative pathogenicity of SARS-CoV-2 Omicron subvariants including BA.1, BA.2, and BA.5. Commun. Biol. *6*, 772.
25. Sano, E., Suzuki, T., Hashimoto, R., Itoh, Y., Sakamoto, A., Sakai, Y., Saito, A., Okuzaki, D., Motooka, D., Muramoto, Y., et al. (2022). Cell response analysis in SARS-CoV-2 infected bronchial organoids. Commun. Biol. *5*, 516.
26. Hashimoto, R., Tamura, T., Watanabe, Y., Sakamoto, A., Yasuhara, N., Ito, H., Nakano, M., Fuse, H., Ohta, A., Noda, T., et al. (2023). Evaluation of Broad Anti-Coronavirus Activity of Autophagy-Related Compounds Using Human Airway Organoids. Mol. Pharm. *20*, 2276–2287.
27. Zahradník, J., Dey, D., Marciano, S., Kolářová, L., Charendoff, C.I., Subtil, A., and Schreiber, G. (2021). A protein-engineered, enhanced yeast display platform for rapid evolution of challenging targets. ACS Synth. Biol. *10*, 3445–3460.
28. Kimura, I., Kosugi, Y., Wu, J., Zahradnik, J., Yamasoba, D., Butlertanaka, E.P., Tanaka, Y.L., Uriu, K., Liu, Y., Morizako, N., et al. (2022). The SARS-CoV-2 Lambda variant exhibits enhanced infectivity and immune resistance. Cell Rep. *38*, 110218.
29. Motozono, C., Toyoda, M., Zahradnik, J., Saito, A., Nasser, H., Tan, T.S., Ngare, I., Kimura, I., Uriu, K., Kosugi, Y., et al. (2021). SARS-CoV-2 spike L452R variant evades cellular immunity and increases infectivity. Cell Host Microbe *29*, 1124–1136.e11.
30. Kimura, I., Yamasoba, D., Tamura, T., Nao, N., Suzuki, T., Oda, Y., Mitoma, S., Ito, J., Nasser, H., Zahradnik, J., et al. (2022). Virological characteristics of the SARS-CoV-2 Omicron BA.2 subvariants, including BA.4 and BA.5. Cell *185*, 3992–4007.e16.
31. Ozono, S., Zhang, Y., Ode, H., Sano, K., Tan, T.S., Imai, K., Miyoshi, K., Kishigami, S., Ueno, T., Iwatani, Y., et al. (2021). SARS-CoV-2 D614G spike mutation increases entry efficiency with enhanced ACE2-binding affinity. Nat. Commun. *12*, 848.
32. Ferreira, I.A.T.M., Kemp, S.A., Datir, R., Saito, A., Meng, B., Rakshit, P., Takaori-Kondo, A., Kosugi, Y., Uriu, K., Kimura, I., et al. (2021). SARS-CoV-2 B.1.617 Mutations L452R and E484Q Are Not Synergistic for Antibody Evasion. J. Infect. Dis. *224*, 989–994.
33. Yamamoto, M., Kiso, M., Sakai-Tagawa, Y., Iwatsuki-Horimoto, K., Imai, M., Takeda, M., Kinoshita, N., Ohmagari, N., Gohda, J., Semba, K., et al. (2020). The anticoagulant nafamostat potently inhibits SARS-CoV-2 S protein-mediated fusion in a cell fusion assay system and viral infection *in vitro* in a cell-yype-dependent manner. Viruses *12*, 629.
34. Kimura, I., Yamasoba, D., Nasser, H., Zahradnik, J., Kosugi, Y., Wu, J., Nagata, K., Uriu, K., Tanaka, Y.L., Ito, J., et al. (2022). The SARS-CoV-2 spike S375F mutation characterizes the Omicron BA.1 variant. iScience *25*, 105720.

35. Meng, B., Abdullahi, A., Ferreira, I.A.T.M., Goonawardane, N., Saito, A., Kimura, I., Yamasoba, D., Gerber, P.P., Fatihi, S., Rathore, S., et al. (2022). Altered TMPRSS2 usage by SARS-CoV-2 Omicron impacts tropism and fusogenicity. Nature *603*, 706–714.

36. Niwa, H., Yamamura, K., and Miyazaki, J. (1991). Efficient selection for high-expression transfectants with a novel eukaryotic vector. Gene *108*, 193–199.

37. Ozono, S., Zhang, Y., Tobiume, M., Kishigami, S., and Tokunaga, K. (2020). Super-rapid quantitation of the production of HIV-1 harboring a luminescent peptide tag. J. Biol. Chem. *295*, 13023–13030.

38. Kondo, N., Miyauchi, K., and Matsuda, Z. (2011). Monitoring viral-mediated membrane fusion using fluorescent reporter methods. Curr. Protoc. Cell Biol. *Chapter 26*, Unit 26.9.

39. Kaku, Y., Kosugi, Y., Uriu, K., Ito, J., Hinay, A.A., Kuramochi, J., Sadamasu, K., Yoshimura, K., Asakura, H., Nagashima, M., et al. (2023). Antiviral efficacy of the SARS-CoV-2 XBB breakthrough infection sera against omicron subvariants including EG.5. Lancet Infect. Dis. *23*, e395–e396.

40. Jackson, B. (2022). gofasta: command-line utilities for genomic epidemiology research. Bioinformatics *38*, 4033–4035.

41. Minh, B.Q., Schmidt, H.A., Chernomor, O., Schrempf, D., Woodhams, M.D., von Haeseler, A., and Lanfear, R. (2020). IQ-TREE 2: New Models and Efficient Methods for Phylogenetic Inference in the Genomic Era. Mol. Biol. Evol. *37*, 1530–1534.

42. Chen, S., Zhou, Y., Chen, Y., and Gu, J. (2018). fastp: an ultra-fast all-in-one FASTQ preprocessor. Bioinformatics *34*, i884–i890.

43. Li, H., and Durbin, R. (2009). Fast and accurate short read alignment with Burrows-Wheeler transform. Bioinformatics *25*, 1754–1760.

44. Li, H., Handsaker, B., Wysoker, A., Fennell, T., Ruan, J., Homer, N., Marth, G., Abecasis, G., and Durbin, R.; 1000 Genome Project Data Processing Subgroup (2009). The sequence alignment/map format and SAMtools. Bioinformatics *25*, 2078–2079.

45. Cingolani, P., Platts, A., Wang le, L., Coon, M., Nguyen, T., Wang, L., Land, S.J., Lu, X., and Ruden, D.M. (2012). A program for annotating and predicting the effects of single nucleotide polymorphisms, SnpEff: SNPs in the genome of Drosophila melanogaster strain w1118; iso-2; iso-3. Fly (Austin) *6*, 80–92.

46. Li, H. (2018). Minimap2: pairwise alignment for nucleotide sequences. Bioinformatics *34*, 3094–3100.

47. Capella-Gutiérrez, S., Silla-Martínez, J.M., and Gabaldón, T. (2009). trimAl: a tool for automated alignment trimming in large-scale phylogenetic analyses. Bioinformatics *25*, 1972–1973.

48. Yu, G. (2020). Using ggtree to visualize data on tree-like structures. Curr. Protoc. Bioinformatics *69*, e96.

49. Khare, S., Gurry, C., Freitas, L., Schultz, M.B., Bach, G., Diallo, A., Akite, N., Ho, J., Lee, R.T., Yeo, W., et al. (2021). GISAID's role in pandemic response. China CDC Wkly. *3*, 1049–1051.

50. Matsuyama, S., Nao, N., Shirato, K., Kawase, M., Saito, S., Takayama, I., Nagata, N., Sekizuka, T., Katoh, H., Kato, F., et al. (2020). Enhanced isolation of SARS-CoV-2 by TMPRSS2-expressing cells. Proc. Natl. Acad. Sci. USA *117*, 7001–7003.

51. Watanabe, Y., Kimura, I., Hashimoto, R., Sakamoto, A., Yasuhara, N., Yamamoto, T., Genotype to Phenotype Japan (G2P-Japan) Consortium, Sato, K., and Takayama, K. (2023). Virological characterization of the 2022 outbreak-causing monkeypox virus using human keratinocytes and colon organoids. J. Med. Virol. *95*, e28827.

52. Dejnirattisai, W., Huo, J., Zhou, D., Zahradník, J., Supasa, P., Liu, C., Duyvesteyn, H.M.E., Ginn, H.M., Mentzer, A.J., Tuekprakhon, A., et al. (2022). SARS-CoV-2 Omicron-B.1.1.529 leads to widespread escape from neutralizing antibody responses. Cell *185*, 467–484.e15.

53. Yamasoba, D., Uriu, K., Plianchaisuk, A., Kosugi, Y., Pan, L., Zahradnik, J., Genotype to Phenotype Japan (G2P-Japan) Consortium, Ito, J., and Sato, K. (2023). Virological characteristics of the SARS-CoV-2 omicron XBB.1.16 variant. Lancet Infect. Dis. *23*, 655–656.

54. Uriu, K., Kimura, I., Shirakawa, K., Takaori-Kondo, A., Nakada, T.A., Kaneda, A., Nakagawa, S., and Sato, K.; Genotype to Phenotype Japan (G2P-Japan) Consortium (2021). Neutralization of the SARS-CoV-2 Mu variant by convalescent and vaccine serum. N. Engl. J. Med. *385*, 2397–2399.

55. MIcochova, P., Kemp, S.A., Dhar, M.S., Papa, G., Meng, B., Ferreira, I.A.T.M., Datir, R., Collier, D.A., Albecka, A., Singh, S., et al. (2021). SARS-CoV-2 B.1.617.2 Delta variant replication and immune evasion. Nature *599*, 114–119.

56. Uriu, K., Cárdenas, P., Muñoz, E., Barragan, V., Kosugi, Y., Shirakawa, K., Takaori-Kondo, A.; Ecuador-COVID19 Consortium, The Genotype to Phenotype Japan (G2P-Japan) Consortium, and Sato, K. (2022). Characterization of the immune resistance of SARS-CoV-2 Mu variant and the robust immunity induced by Mu infection. J. Infect. Dis. *226*, 1200–1203.

57. Ikeda, T., Shimizu, R., Nasser, H., Carpenter, M.A., Cheng, A.Z., Brown, W.L., Sauter, D., and Harris, R.S. (2023). APOBEC3 degradation is the primary function of HIV-1 Vif determining virion infectivity in the myeloid cell line THP-1. mBio *14*, e0078223.

58. Nasser, H., Shimizu, R., Ito, J., Genotype to Phenotype Japan (G2P-Japan) Consortium, Saito, A., Sato, K., and Ikeda, T. (2022). Monitoring fusion kinetics of viral and target cell membranes in living cells using a SARS-CoV-2 spike-protein-mediated membrane fusion assay. Star Protoc. *3*, 101773.

59. Reed, L.J., and Muench, H. (1938). A simple method of estimating fifty percent endpoints. Am. J. Hyg. *27*, 493–497.

60. Deguchi, S., Tsuda, M., Kosugi, K., Sakamoto, A., Mimura, N., Negoro, R., Sano, E., Nobe, T., Maeda, K., Kusuhara, H., et al. (2021). Usability of polydimethylsiloxane-based microfluidic devices in pharmaceutical research using human hepatocytes. ACS Biomater. Sci. Eng. *7*, 3648–3657.

STAR★METHODS

KEY RESOURCES TABLE

REAGENT or RESOURCE	SOURCE	IDENTIFIER
Antibodies		
Rabbit anti-SARS-CoV-2 S polyclonal antibody	Novus Biologicals	Cat# NB100-56578; RRID: AB_838846
Mouse anti-HIV-1 p24 monoclonal antibody	HIV Reagent Program	Cat# 183-H12-5C; RRID: AB_2819250
Mouse anti-α tubulin monoclonal antibody	Sigma-Aldrich	Cat# T5168; RRID: AB_477579
Goat anti-rabbit secondary HRP conjugate	Proteinsimple	Cat# 042-206; RRID: AB_2860577
Goat anti-mouse secondary HRP conjugate	Psroteinsimple	Cat# 042-205; RRID: AB_2860576
Rabbit anti-SARS-CoV-2 S S1/S2 polyclonal antibody	Thermo Fisher Scientific	Cat# PA5-112048; RRID: AB_2866784
Normal rabbit IgG	Southern Biotech	Cat# 0111-01; RRID: AB_2732899
APC-conjugated goat anti-rabbit IgG polyclonal antibody	Jackson ImmunoResearch	Cat# 111-136-144; RRID: AB_2337987
Rabbit anti-SARS-CoV-2 N poly-clonal antibody	GeneTex	Cat# GTX135570; RRID: AB_2887498
Alexa 488-conjugated anti-rabbit IgG antibody	Thermo Fisher Scientific	Cat# A-11008; RRID: AB_143165
Mouse anti-SARS-CoV-2 N monoclonal antibody	R&D Systems	Cat# MAB10474-SP; RRID: N/A
Envision FLEX, High pH	Agilent Technologies	Cat# K8000 RRID: N/A
Bacterial and virus strains		
SARS-CoV-2 BA.2 (strain TY40-385)	Kimura et al.[22] and Tamura et al.[24]	N/A
SARS-CoV-2 EG.5.1 (strain KU2023071028)	Tsujino et al.[18]	N/A
SARS-CoV-2 BA.2.86 (strain TKYnat15020)	This study	N/A
Biological samples		
Human sera	This study	N/A
Human airway organoids	Sano et al.[25]	N/A
Airway-on-a-chips	Hashimoto et al.[20]	N/A
Human iPSC-derived lung organoids	Hashimoto et al.[26]	N/A
Chemicals, peptides, and recombinant proteins		
TransIT-LT1	Takara	Cat# MIR2300
TransIT-293 transfection reagent	Mirus	Cat# MIR2704
Recombinant RNase inhibitor	Takara	Cat# 2313B
Fetal bovine serum	Sigma-Aldrich	Cat# 172012-500ML
Penicillin-streptomycin	Sigma-Aldrich	Cat# P4333-100ML
DMEM (high glucose)	Sigma-Aldrich	Cat# 6429-500ML
DMEM (high glucose)	Nacalai Tesque	Cat# 08458-16
DMEM (low glucose)	Wako	Cat# 041-29775
EMEM	Sigma-Aldrich	Cat# M4655-500ML
EMEM	Wako	Cat# 056-08385
EGM-2-MV medium	Lonza	Cat# CC-3202
DMEM/F12 medium	Thermo Fisher Scientific	Cat# 11320033
SD-CAA medium	Zahradník et al.[27]	N/A
1/9 medium	Zahradník et al.[27]	N/A
Glucose	Sigma-Aldrich	Cat# G8270
Galactose	Sigma-Aldrich	Cat# G0750

(*Continued on next page*)

Continued

REAGENT or RESOURCE	SOURCE	IDENTIFIER
Yeast nitrogen base	Sigma-Aldrich	Cat# Y0626
Casamino acids	Sigma-Aldrich	Cat# 2240
Sodium phosphate dibasic	Sigma-Aldrich	Cat# S9763
Sodium phosphate monobasic	Sigma-Aldrich	Cat# S3139
CF®640R Succinimidyl Ester	Biotium	Cat# BT92108
PneumaCult ALI medium	STEMCELL Technologies	Cat# ST-05001
G418	Nacalai Tesque	Cat# G8168-10ML
N2	FUJIFILM Wako Pure Chemical	Cat# 141-08941
B-27 Supplement Minus Vitamin A	Thermo Fisher Scientific	Cat# 12587001
ascorbic acid	STEMCELL Technologies	Cat# ST-72132
GlutaMAX	Thermo Fisher Scientific	Cat# 35050-079
1% monothioglycerol	FUJIFILM Wako Pure Chemical	Cat# 195-15791
recombinant Activin A	R&D Systems	Cat# 338-AC-010
dorsomorphin dihydrochloride	FUJIFILM Wako Pure Chemical	Cat# 047-33763
SB431542	FUJIFILM Wako Pure Chemical	Cat# 037-24293
IWP2	Stemolecule	Cat# 04-0034
CHIR99021	FUJIFILM Wako Pure Chemical	Cat# 032-23104
human FGF10	PeproTech	Cat# 100-26
human FGF7	PeproTech	Cat# 100-19
human BMP4	PeproTech	Cat# 120-05ET
human EGF	PeproTech	Cat# AF-100-15
all-trans retinoic acid	Sigma-Aldrich	Cat# R2625
dexamethasone	Selleck	Cat# S1322
8-bromo-cAMP	Sigma-Aldrich	Cat# B7880
IBMX	FUJIFILM Wako Pure Chemical	Cat# 099-03411
KpnI	New England Biolab	Cat# R0142S
NotI	New England Biolab	Cat# R1089S
Fibronectin	Sigma-Aldrich	Cat# F1141
Matrigel growth factor reduced basement membrane	Corning	Cat# 354230
Triton X-100	Nacalai Tesque	Cat# 35501-15
EnduRen live cell substrate	Promega	Cat# E6481
Soluble human ACE2 (residues 18-618 for binding assay)	Yamasoba et al.[10]	N/A
SARS-CoV-2 B.1.1 S RBD	Kimura et al.[28] and Motozono et al.[29]	N/A
SARS-CoV-2 BA.2 S RBD	Kimura et al.[30]	N/A
SARS-CoV-2 XBB.1 S RBD	Tamura et al.[23]	N/A
SARS-CoV-2 XBB.1.5 S RBD	Uriu et al.[14]	N/A
SARS-CoV-2 BA.2.86 S RBD	This study	N/A
SARS-CoV-2 S RBD derivatives, see Figure 2A	This study	N/A
Bilirubin	Sigma-Aldrich	Cat# 14370-1G
Medetomidine hydrochloride (Domitor®)	Nippon Zenyaku Kogyo	N/A
Midazolam	Fujifilm Wako	Cat# 135-13791
Butorphanol (Vetorphale®)	Meiji Seika Pharma	N/A
Alphaxaone (Alfaxan®)	Jurox	N/A
Remdesivir	Clinisciences	Cat# A17170
EIDD-1931	Cell Signalling Technology	Cat# 81178S
Nirmatrelvir	MedChemExpress	Cat# HY-138687

(*Continued on next page*)

Continued

REAGENT or RESOURCE	SOURCE	IDENTIFIER
Ensitrelvir	MedChemExpress	Cat# HY-143216
n-octyl-β-D-glucoside	Dojindo	Cat# O001
Nonidet P40 substitute	Nacalai Tesque	Cat# 18558-54
Protease inhibitor cocktail	Nacalai Tesque	Cat# 03969-21
Protein assay dye	Bio-Rad	Cat# 5000006
Sample buffer	proteinsimple	Cat# 99351
5 × Fluorescent Master mix	proteinsimple	Cat# PS-ST01EZ-8
PBS	Nacalai Tesque	Cat# 09154-85
Critical commercial assays		
QIAamp viral RNA mini kit	Qiagen	Cat# 52906
NEBNext Ultra RNA Library Prep Kit for Illumina	New England Biolabs	Cat# E7530
MiSeq reagent kit v3	Illumina	Cat# MS-102-3001
One Step TB Green PrimeScript PLUS RT-PCR kit	Takara	Cat# RR096A
SARS-CoV-2 direct detection RT-qPCR kit	Takara	Cat# RC300A
Nano Glo HiBiT lytic detection system	Promega	Cat# N3040
Bright-Glo luciferase assay system	Promega	Cat# E2650
Deposited data		
Viral genome sequencing data of working viral stocks (see also Table S4)	This study	SRA: PRJDB14324(https://www.ncbi.nlm.nih.gov/sra)
Experimental models: Cell lines		
Human: HEK293T cells	ATCC	CRL-3216
Human: HEK293 cells	ATCC	CRL-1573
LentiX-293T	TaKaRa	Cat# 632180
Human: HOS-ACE2/TMPRSS2 cells	Ozono et al.[31]; Ferreira et al.[32]	N/A
Human: Calu-3 cells	ATCC	HTB-55
Human: Calu-3/DSP$_{1-7}$ cells	Yamamoto et al.[33]	N/A
African green monkey (*Chlorocebus sabaeus*): Vero cells	JCRB Cell Bank	JCRB0111
African green monkey (*Chlorocebus sabaeus*): VeroE6/TMPRSS2 cells	JCRB Cell Bank	JCRB1819
Yeast (*Saccharomyces cerevisiae*): strain EBY100	ATCC	MYA-4941
Experimental models: Organisms/strains		
Human lung microvascular endothelial cells (HMVEC-L)	Lonza	Cat# CC-2527
Slc:Syrian hamsters (male, 4 weeks old)	Japan SLC Inc.	http://www.jslc.co.jp/pdf/hamster/2020/028_Slc_Syrian.pdf
Oligonucleotides		
Primers for the construction of plasmids expressing the codon-optimized S proteins of BA.2-bearing variants, see Table S3	This study	N/A
RT-qPCR, forward: AGC CTC TTC TCG TTC CTC ATC AC	Yamasoba et al.[10]; Saito et al.[11]; Ito et al.[15]; Saito et al.[19]; Suzuki et al.[21]; Tamura et al.[23]; Kimura et al.[30]; Kimura et al.[34]; Motozono et al.[29]; Meng et al.[35]	N/A
RT-qPCR, reverse: CCG CCA TTG CCA GCC ATT C	Yamasoba et al.[10]; Saito et al.[11]; Ito et al.[15]; Saito et al.[19]; Suzuki et al.[21]; Tamura et al.[23]; Kimura et al.[30]; Kimura et al.[34]; Motozono et al.[29]; Meng et al.[35]	N/A

(*Continued on next page*)

Continued

REAGENT or RESOURCE	SOURCE	IDENTIFIER
Primers for the construction of yeast-optimized SARS-CoV-2 BA.2 RBD expression plasmid, see Table S3	This study	N/A
Recombinant DNA		
Plasmid: pCAGGS	Niwa et al.[36]	N/A
Plasmid: psPAX2-IN/HiBiT	Ozono et al.[37]	N/A
Plasmid: pWPI-Luc2	Ozono et al.[37]	N/A
Plasmid: pJYDC1	Addgene	Cat# 162458
Plasmid: $pDSP_{8-11}$	Kondo et al.[38]	N/A
Plasmid: pC-B.1.1 S	Ozono et al.[31]; Motozono et al.[29]	N/A
Plasmid: pC-BA.2 S	Yamasoba et al.[10]	N/A
Plasmid: pC-EG5.1 S	Kaku et al.[39]	N/A
Plasmid: pC-XBB.1.5 S	Uriu et al.[14]	N/A
Plasmid: pC-BA.2.86 S	This study	N/A
Plasmid: pC-BA.2 ins16MPLF S	This study	N/A
Plasmid: pC-BA.2 R21T S	This study	N/A
Plasmid: pC-BA.2 S50L S	This study	N/A
Plasmid: pC-BA.2 HV69-70del S	Kimura et al.[30]	N/A
Plasmid: pC-BA.2 V127F S	This study	N/A
Plasmid: pC-BA.2 Y144del S	Tamura et al.[23]	N/A
Plasmid: pC-BA.2 F157S S	This study	N/A
Plasmid: pC-BA.2 R158G S	This study	N/A
Plasmid: pC-BA.2 N211del S	This study	N/A
Plasmid: pC-BA.2 L212I S	This study	N/A
Plasmid: pC-BA.2 L216F S	This study	N/A
Plasmid: pC-BA.2 H245N S	This study	N/A
Plasmid: pC-BA.2 A264D S	This study	N/A
Plasmid: pC-BA.2 I332V S	This study	N/A
Plasmid: pC-BA.2 D339H S	Saito et al.[11]	N/A
Plasmid: pC-BA.2 K356T S	This study	N/A
Plasmid: pC-BA.2 R403K S	This study	N/A
Plasmid: pC-BA.2 V445H S	This study	N/A
Plasmid: pC-BA.2 G446S S	Saito et al.[11]	N/A
Plasmid: pC-BA.2 N450D S	This study	N/A
Plasmid: pC-BA.2 L452W S	This study	N/A
Plasmid: pC-BA.2 N460K S	Saito et al.[11]	N/A
Plasmid: pC-BA.2 N481K S	This study	N/A
Plasmid: pC-BA.2 V483del S	This study	N/A
Plasmid: pC-BA.2 A484K S	This study	N/A
Plasmid: pC-BA.2 F486P S	This study	N/A
Plasmid: pC-BA.2 R493Q S	Kimura et al.[30]	N/A
Plasmid: pC-BA.2 E554K S	This study	N/A
Plasmid: pC-BA.2 A570V S	This study	N/A
Plasmid: pC-BA.2 P621S S	This study	N/A
Plasmid: pC-BA.2 H681R S	This study	N/A
Plasmid: pC-BA.2 S939F S	This study	N/A
Plasmid: pC-BA.2 P1143L S	This study	N/A
Plasmid: pJYDC1-RBD-BA-2-86 K403R	This study	N/A
Plasmid: pJYDC1-RBD-BA-2-86 H445V	This study	N/A
Plasmid: pJYDC1-RBD-BA-2-86 D450N	This study	N/A

(*Continued on next page*)

Continued

REAGENT or RESOURCE	SOURCE	IDENTIFIER
Plasmid: pJYDC1-RBD-BA-2-86 W452L	This study	N/A
Plasmid: pJYDC1-RBD-BA-2-86 K481N	This study	N/A
Plasmid: pJYDC1-RBD-BA-2-86 del483V	This study	N/A
Plasmid: pJYDC1-RBD-WT R403K	This study	N/A
Plasmid: pJYDC1-RBD-WT V445H	This study	N/A
Plasmid: pJYDC1-RBD-WT N450D	This study	N/A
Plasmid: pJYDC1-RBD-WT L452W	This study	N/A
Plasmid: pJYDC1-RBD-WT N481K	This study	N/A
Plasmid: pJYDC1-RBD-WT V483del	This study	N/A
Plasmid: pJYDC1-RBD-BA2 R403K	This study	N/A
Plasmid: pJYDC1-RBD-BA2 V445H	This study	N/A
Plasmid: pJYDC1-RBD-BA2 N450D	This study	N/A
Plasmid: pJYDC1-RBD-BA2 L452W	This study	N/A
Plasmid: pJYDC1-RBD-BA2 N481K	This study	N/A
Plasmid: pJYDC1-RBD-BA2 V483del	This study	N/A
Plasmid: pJYDC1-RBD-XBB-1-5 R403K	This study	N/A
Plasmid: pJYDC1-RBD-XBB-1-5 P445H	This study	N/A
Plasmid: pJYDC1-RBD-XBB-1-5 N450D	This study	N/A
Plasmid: pJYDC1-RBD-XBB-1-5 L452W	This study	N/A
Plasmid: pJYDC1-RBD-XBB-1-5 N481K	This study	N/A
Plasmid: pJYDC1-RBD-XBB-1-5 V483del	This study	N/A
Plasmid: pJYDC1-RBD-XBB R403K	This study	N/A
Plasmid: pJYDC1-RBD-XBB P445H	This study	N/A
Plasmid: pJYDC1-RBD-XBB N450D	This study	N/A
Plasmid: pJYDC1-RBD-XBB L452W	This study	N/A
Plasmid: pJYDC1-RBD-XBB N481K	This study	N/A
Plasmid: pJYDC1-RBD-XBB V483del	This study	N/A
Software and algorithms		
Nextclade v2.14.0 CLI workflow	Hadfield et al.[12]	https://clades.nextstrain.org/ https://github.com/nextstrain/nextclade
gofasta v1.2.0	Jackson[40]	https://github.com/virus-evolution/gofasta
IQTree v2.2.2.6	Minh et al.[41]	https://github.com/iqtree/iqtree2
fastp v0.21.0	Chen et al.[42]	https://github.com/OpenGene/fastp
BWA-MEM v0.7.17	Li and Durbin[43]	http://bio-bwa.sourceforge.net
SAMtools v1.9	Li et al.[44]	http://www.htslib.org
snpEff v5.0e	Cingolani et al.[45]	http://pcingola.github.io/SnpEff
Minimap2 v2.24	Li[46]	https://github.com/lh3/minimap2
trimAl v1.2	Capella-Gutiérrez et al.[47]	http://trimal.cgenomics.org
CmdStan v2.33.1	The Stan Development Team	https://mc-stan.org
CmdStanr v0.6.1	The Stan Development Team	https://mc-stan.org/cmdstanr/
R v4.3.1	The R Foundation	https://www.r-project.org/
ggtree v3.8.2	Yu[48]	https://github.com/YuLab-SMU/ggtree
Sequencher v5.1 software	Gene Codes Corporation	N/A
In-house scripts	This study	https://github.com/TheSatoLab/BA.2.86_full
Prism 9 software v9.1.1	GraphPad Software	https://www.graphpad.com/scientific-software/prism/
Fiji software v2.2.0	ImageJ	https://fiji.sc
FlowJo software v10.7.1	BD Biosciences	https://www.flowjo.com/solutions/flowjo
Python v3.7 and v3.11	Python Software Foundation	https://www.python.org

(*Continued on next page*)

Continued

REAGENT or RESOURCE	SOURCE	IDENTIFIER
FinePointe Station and Review softwares v2.9.2.12849	DSI	https://www.datasci.com/products/software/finepointe-software
NDP.scan software v3.2.4	Hamamatsu Photonics	https://nanozoomer.hamamatsu.com/jp/en/why_nanozoomer/scan.html
Compass for Simple Western v6.1.0	Proteinsimple	N/A
BZ-X800 Analyzer software	Keyence	N/A
Other		
Centro XS3 LB960	Berthhold Technologies	N/A
GloMax explorer multimode microplate reader 3500	Promega	N/A
CytoFLEX Flow Cytometer	Beckman Coulter	N/A
GISAID database	Khare et al.[49]	https://www.gisaid.org/
96-well black plate	PerkinElmer	Cat# 6005225
3,3'-diaminobenzidine tetrahydrochloride	Dako	Cat# DM827
MAS-GP-coated glass slides	Matsunami Glass	Cat# S9901
A1Rsi Confocal Microscope	Nikon	N/A
QuantStudio 3 Real-Time PCR system	Thermo Fisher Scientific	N/A
CFX Connect Real-Time PCR Detection system	Bio-Rad	N/A
Eco Real-Time PCR System	Illumina	N/A
qTOWER3 G Real-Time System	Analytik Jena	N/A
7500 Real-Time PCR System	Thermo Fisher Scientific	N/A
CytoFLEX S Flow Cytometer	Beckman Coulter	Cat# N0-V4-B2-Y4
Autostainer Link 48	Dako	N/A
Buxco Small Animal Whole Body Plethysmography	DSI	https://www.datasci.com/products/buxco-respiratory-products/finepointe-whole-body-plethysmography
PDMS (Silicone Elastomer Kit)	Dow Corning	Cat# SYLGARD 184
SU-8 2150	MicroChem	Cat# SU-8 2150
Kai Medical Biopsy Punch 6mm	Kai Corporation	Cat# BP-L60K
Cell Culture Inserts, 3.0-μm pore size inserts, 6-well, Transparent PET	Falcon	Cat# 353091
Abby	proteinsimple	N/A
All-in-One Fluorescence Microscope BZ-X800	Keyence	N/A

RESOURCE AVAILABILITY

Lead contact

Further information and requests for resources and reagents should be directed to and will be fulfilled by the lead contact, Kei Sato (keisato@g.ecc.u-tokyo.ac.jp).

Materials availability

All unique reagents generated in this study are listed in the key resources table and available from the lead contact with a completed Materials Transfer Agreement.

Data and code availability

- All databases/datasets used in this study are available from GenBank database (https://www.ncbi.nlm.nih.gov/genbank/) the GISAID database (https://www.gisaid.org; EPI_SET_230919bh; EPI_SET_231129nz).
- Computational codes used in this study are available on the GitHub repository (https://github.com/TheSatoLab/BA.2.86_full).
- Any additional information required to reanalyze the data reported in this work is available from the lead contact upon request.

EXPERIMENTAL MODEL AND SUBJECT DETAILS

Ethics statement

All experiments with hamsters were performed in accordance with the Science Council of Japan's Guidelines for the Proper Conduct of Animal Experiments. The protocols were approved by the Institutional Animal Care and Use Committee of National University Corporation Hokkaido University (approval ID: 20-0123 and 20-0060). All protocols involving specimens from human subjects recruited at Interpark Kuramochi Clinic were reviewed and approved by the Institutional Review Board of Interpark Kuramochi Clinic (approval ID: G2021-004). All human subjects provided written informed consent. All protocols for the use of human specimens were reviewed and approved by the Institutional Review Boards of The Institute of Medical Science, The University of Tokyo (approval IDs: 2021-1-0416 and 2021-18-0617).

Human serum collection

Convalescent sera were collected from fully vaccinated individuals who had been infected with BA.2 (9 2-dose vaccinated and 4 3-dose vaccinated; 11–61 days after testing. n=13 in total; average age: 45 years, range: 24–82 years, 62% male) (Figure S2F), and fully vaccinated individuals who had been infected with BA.5 (1 2-dose vaccinated, 15 3-dose vaccinated and 1 4-dose vaccinated; 10–23 days after testing. n=17 in total; average age: 52 years, range: 25–73 years, 53% male) (Figure S2G). The SARS-CoV-2 variants were identified as previously described.[10,22] Sera were inactivated at 56°C for 30 minutes and stored at –80°C until use. The details of the convalescent sera are summarized in Table S2.

Cell culture

HEK293T cells (a human embryonic kidney cell line; ATCC, CRL-3216), HEK293 cells (a human embryonic kidney cell line; ATCC, CRL-1573), LentiX-293T (a derivative of HEK293T cells for superior lentivirus packaging; TaKaRa, Cat# 632180) and HOS-ACE2/TMPRSS2 cells (HOS cells stably expressing human ACE2 and TMPRSS2)[31,32] were maintained in DMEM (high glucose) (Sigma-Aldrich, Cat# 6429-500ML) containing 10% fetal bovine serum (FBS, Sigma-Aldrich Cat# 172012-500ML) and 1% penicillin–streptomycin (PS) (Sigma-Aldrich, Cat# P4333-100ML). Calu-3 cells (ATCC, HTB-55) were maintained in Eagle's minimum essential medium (EMEM) (Sigma-Aldrich, Cat# M4655-500ML) containing 10% FBS and 1% PS. Calu-3/DSP_{1-7} cells (Calu-3 cells stably expressing DSP_{1-7})[33] were maintained in EMEM (Wako, Cat# 056-08385) containing 20% FBS and 1% PS. Vero cells [an African green monkey (Chlorocebus sabaeus) kidney cell line; JCRB Cell Bank, JCRB0111] were maintained in Eagle's minimum essential medium (EMEM) (Sigma-Aldrich, Cat#M4655-500ML) containing 10% FBS and 1% PS. VeroE6/TMPRSS2 cells (VeroE6 cells stably expressing human TMPRSS2; JCRB Cell Bank, JCRB1819)[50] were maintained in DMEM (low glucose) (Wako, Cat#041-29775) containing 10% FBS, G418 (1 mg/ml; Nacalai Tesque, Cat#G8168-10ML) and 1% PS. Airway organoids-derived air-liquid interface (AO-ALI) model,[25] and human iPSC-derived colon organoids[51] were generated as previously described.

Human lung organoids

Human iPSC-derived lung organoids were generated as previously described.[26] Human iPSCs were seeded onto Matrigel Growth Factor Reduced Basement Membrane (Corning, Cat# 354230)-coated cell culture plates (2.0×10^5 cells/4 cm^2) and cultured for 2 d. Lung organoids differentiation was performed in serum-free differentiation (SFD) medium of DMEM/F12 (3:1) (Thermo Fisher Scientific, Cat# 11320033) supplemented with N2 (FUJIFILM Wako Pure Chemical, Cat# 141-08941), B-27 Supplement Minus Vitamin A (Thermo Fisher Scientific, Cat# 12587001), ascorbic acid (50 μg/ml, STEMCELL Technologies, Cat# ST-72132), 1× GlutaMAX (Thermo Fisher Scientific, Cat# 35050-079), 1% monothioglycerol (FUJIFILM Wako Pure Chemical, Cat# 195-15791), 0.05% bovine serum albumin, and 1× penicillin–streptomycin. For definitive endoderm induction, the cells were cultured for 3 d (days 0–3) using SFD medium supplemented with 10 μM Y-27632 and 100 ng/ml recombinant Activin A (R&D Systems, Cat# 338-AC-010). For anterior foregut endoderm induction (days 3–5), the cells were cultured in SFD medium supplemented with 1.5 μM dorsomorphin dihydrochloride (FUJIFILM Wako Pure Chemical, Cat# 047-33763) and 10 μM SB431542 (FUJIFILM Wako Pure Chemical, Cat# 037-24293) for 24 h and then in SFD medium supplemented with 10 μM SB431542 and 1 μM IWP2 (Stemolecule, Cat# 04-0034) for another 24 h. For the induction of lung progenitors (days 5–12), the resulting anterior foregut endoderm was cultured with SFD medium supplemented with 3 μM CHIR99021 (FUJIFILM Wako Pure Chemical, Cat# 032-23104), 10 ng/ml human FGF10 (PeproTech, Cat# 100-26), 10 ng/ml human FGF7 (PeproTech, Cat# 100-19), 10 ng/ml human BMP4 (PeproTech, Cat# 120-05ET), 20 ng/ml human EGF (PeproTech, Cat# AF-100-15), and all-trans retinoic acid (ATRA, Sigma-Aldrich, Cat# R2625) for 7 d. At day 12 of differentiation, the cells were dissociated and embedded in Matrigel Growth Factor Reduced Basement Membrane to generate organoids. For lung organoid maturation (days 12–30), the cells were cultured in SFD medium containing 3 μM CHIR99021, 10 ng/mL human FGF10, 10 ng/mL human FGF7, 10 ng/ml human BMP4, and 50 nM ATRA for 8 d. At day 20 of differentiation, the lung organoids were recovered from the Matrigel, and the resulting suspension of lung organoids was seeded onto Matrigel-coated 96-well cell culture plates. The organoids were cultured in SFD medium containing 50 nM dexamethasone (Selleck, Cat# S1322), 0.1 mM 8-bromo-cAMP (Sigma-Aldrich, Cat# B7880), and 0.1 mM IBMX (3-isobutyl-1-methylxanthine) (FUJIFILM Wako Pure Chemical, Cat# 099-03411) for an additional 10 d.

Animal experiments

Animal experiments (Figure 4) were performed as previously described.[10,11,15,17–19,21–23,34] Syrian hamsters (male, 4 weeks old) were purchased from Japan SLC Inc. (Shizuoka, Japan). Baseline body weights were measured before infection. For the virus infection experiments, hamsters were anaesthetized by intramuscular injection of a mixture of either 0.15 mg/kg medetomidine hydrochloride (Domitor®, Nippon Zenyaku Kogyo), 2.0 mg/kg midazolam (FUJIFILM Wako Chemicals, Cat# 135-13791) and 2.5 mg/kg butorphanol (Vetorphale®, Meiji Seika Pharma), or 0.15 mg/kg medetomidine hydrochloride, 2.0 mg/kg alphaxaone (Alfaxan®, Jurox) and 2.5 mg/kg butorphanol. Clinical isolates of SARS-CoV-2 (BA.2.86, BA.2, and EG.5.1) (2,000 $TCID_{50}$ in 100 μl), or medium (100 μl) were intranasally inoculated under anesthesia. Oral swabs were collected at 2 and 5 d.p.i. Body weight, enhanced pause (Penh) and the ratio of time to peak expiratory follow relative to the total expiratory time (Rpef) were routinely monitored at indicated time-points (see "lung function test" section below). Respiratory organs were anatomically collected at 1, 3 and 5 d.p.i (for lung) or 1 d.p.i. (for trachea). Viral RNA load in the respiratory tissues and oral swab were determined by RT–qPCR. The respiratory tissues were also used for histopathological and IHC analyses (see "H&E staining" and "IHC" sections below).

METHOD DETAILS

Phylogenetic analysis

A total of 15,991,922 SARS-CoV-2 genome sequences and their metadata were downloaded from the GISAID database with a released date of September 14, 2023 (https://www.gisaid.org/). To prepare dataset for lineages other than BA.2.86, the dataset was then filtered based on the following criteria: (i) retained only distinct Accession IDs, (ii) host labeled as 'Human', (iii) the collection date recorded, (iv) the PANGO lineage column should not be empty, none or unassigned, and (v) retained sequences with less than 1% proportion of ambiguous bases. We assigned Nextclade clade information to individual viral sequences using the Nextclade v2.14.0 CLI workflow (https://clades.nextstrain.org/). Subsequently, we randomly sampled 20 sequences from each Nextclade clade. To prepare dataset for BA.2.86 (including BA.2.86.1), we extracted sequences in which PANGO lineage is BA.2.86 or BA.2.86.1 from the GISAID metadata. Subsequently, we applied the same filtering criteria as mentioned above (i-iv) and additionally set the threshold for ambiguous bases below 3%. We set this relaxed threshold for BA.2.86 because most of BA.2.86 sequences have a large undetermined regions just before S gene due to the presence of mutations in the primer site. After the filtering, 89 sequences of BA.2.86 were included in the final dataset.

To construct the phylogenetic tree, viral genome sequences (EPI SET ID: EPI_SET_230919bh) were mapped and aligned to the reference sequence of Wuhan-Hu-1 (GenBank accession number: NC_045512.2) through minimap v2.24,[46] and the resulting sam format file was converted to fasta format using gofasta v1.2.0.[40] During this conversion, the alignment sites corresponding to 1–265 and 29674–9903 positions on the reference genome were masked, typically converted to 'NNN'. Alignment sites with more than 10% of sequences containing gaps or uncertain nucleotides were subjected to trimming using trimAl v1.2.[47] Phylogenetic tree construction was accomplished via the three-step protocol: (i) the initial tree was constructed, (ii) the external branch lengths of the initial tree were filtered using Grubb's test and the *p value* threshold was set to 1.0E-5 enabling those tips with longer external branch to be removed, (iii) the final tree was constructed with the similar parameter as the initial tree.[15] A maximum likelihood (ML) phylogenetic tree of the genome was inferred by IQTree v2.2.2.6 with the GTR nucleotide substitution model.[41] The node support value was computed by 1000 bootstrap iterations. The visualization of the final tree was generated in R v4.3.1 using ggtree v3.8.2.[48]

Epidemic dynamics analysis

To estimate the global average and country-specific R_e values of SARS-CoV-2 lineages, we analyzed the GISAID genome surveillance data spanning from April 1, 2023 to November 15, 2023. Genomic and surveillance data of 16,256,454 sequences with a released date of November 27, 2023, were acquired from the GISAID database (https://www.gisaid.org/). We excluded the sequence records with the following features: i) a lack of collection date information; ii) sampling in animals other than humans; iii) sampling by quarantine; or iv) without the PANGO lineage information. We then allocated Nextclade clade information to individual viral sequences using the Nextclade v2.14.0 CLI workflow (https://clades.nextstrain.org/). For the definition of lineages other than BA.2.86, we used the Nextclade clade classification: 23A (XBB.1.5), 23B (XBB.1.16), and 23F (EG.5.1). Since BA.2.86 and its sublineages has not been annotated in the Nextclade clade, we instead used the Nextclade PANGO lineage classification assigned by Nextclade for these lineages. BA.2.86 sublineages (e.g., BA.2.86.1) are summarized as BA.2.86. From the BA.2.86 sequences, we excluded sequences that were assigned as JN.1 and JQ.1, which are BA.2.86 sublineages harbouring additional spike mutations (S:L455S for JN.1, and S:T95I for JQ.1). Also, we excluded other sequences with either of these mutations. We then analyzed the datasets of the countries with $\geq$100 available BA.2.86 sequences: Australia, Belgium, Canada, Denmark, France, Germany, Iceland, Japan, Netherlands, Spain, Sweden, Switzerland, United Kingdom and USA (analyzed dataset: EPI_SET_231129nz). Subsequently, we counted the daily frequency of each viral lineage in each country and fit a Bayesian hierarchical multinomial logistic model[10,11] to the lineage frequency data to estimate the global average and country-specific R_e of the lineages. The relative R_e of each viral lineage l in each county s (r_{ls}) was calculated according to the country-specific slope parameter, β_{ls}, as $r_{ls} = exp(\gamma\beta_{ls})$ where γ is the average viral generation time (2.1 days)(http://sonorouschocolate.com/covid19/index.php?title=Estimating_Generation_Time_Of_Omicron). Similarly, the global average relative R_e of each viral lineage was calculated according to the global average slope parameter, β_l, as $r_l = exp(\gamma\beta_l)$. For parameter estimation, the intercept and slope parameters of the EG.5.1 were set at 0. As a result, the relative R_e of EG.5.1 was fixed at 1, and the R_e of other viral lineages were estimated relative to that of EG.5.1. Parameter estimation was

conducted via the MCMC method implemented in CmdStan v2.33 (https://mc-stan.org) with CmdStanr v0.6.1 (https://mc-stan.org/cmdstanr/). Four separate MCMC chains were executed, consisting of 1,000 steps as the warmup iterations, and 2,000 steps as the sampling iterations. We verified the successful convergence of our MCMC runs by assuring that all the estimated parameters had showed <1.01 R-hat convergence diagnostic values and >200 effective sampling size values. Information on the estimated parameters is summarized in Table S1.

Viral genome sequencing

Viral genome sequencing was performed as previously described.[22] Briefly, the virus sequences were verified by viral RNA-sequencing analysis. Viral RNA was extracted using a QIAamp viral RNA mini kit (Qiagen, Cat# 52906). The sequencing library employed for total RNA sequencing was prepared using the NEBNext Ultra RNA Library Prep Kit for Illumina (New England Biolabs, Cat# E7530). Paired-end 76-bp sequencing was performed using a MiSeq system (Illumina) with MiSeq reagent kit v3 (Illumina, Cat# MS-102-3001). Sequencing reads were trimmed using fastp v0.21.0[42] and subsequently mapped to the viral genome sequences of a lineage B isolate (strain Wuhan-Hu-1; GenBank accession number: NC_045512.2)[50] using BWA-MEM v0.7.17.[43] Variant calling, filtering, and annotation were performed using SAMtools v1.9[44] and snpEff v5.0e.[45]

Plasmid construction

Plasmids expressing the codon-optimized SARS-CoV-2 S proteins of B.1.1 (the parental D614G-bearing variant), BA.2, XBB.1.5,[14] EG.5.1, and BA.2.86 were prepared in our previous studies.[2,18,22] Plasmids expressing the codon-optimized S proteins of BA.2.86 and BA.2 S-based derivatives were generated by site-directed overlap extension PCR using the primers listed in Table S3. The resulting PCR fragment was digested with KpnI (New England Biolabs, Cat# R0142S) and NotI (New England Biolabs, Cat# R1089S) and inserted into the corresponding site of the pCAGGS vector.[36] Nucleotide sequences were determined by DNA sequencing services (Eurofins), and the sequence data were analyzed by Sequencher v5.1 software (Gene Codes Corporation).

Yeast surface display analysis

Utilizing yeast surface display (Figure 2A), we conducted an analysis of the interaction between selected RBD variants and mACE2, following established protocols.[11,13–15,18,23,52,53] The pJYDC plasmids bearing SARS-CoV-2_RBD-WT, BA2 XBB, XBB.1.5, XBB.1.16 and EG.5.1 variants were used in our previous research.[2,10,14,18,23,39,53] The gene for RBD-BA.2.86 with *S. cerevisiae* codon usage was obtained from Twist Biosciences. The mutations in RBDs were incorporated by restriction-free cloning. All PCR reactions were conducted using the KAPA HiFi HotStart ReadyMix kit (Roche, Cat# KK2601) and the pJYDC1 plasmid (Addgene, Cat# 162458), as previously outlined.[2,10,14,18,23,39,53] A detailed list of the primers used can be found in Table S3. Verified plasmids were transformed into yeast Saccharomyces cerevisiae strain EBY100 (ATCC, MYA-4941) through electroporation and selected on SD-Trp selection plates. Yeast colonies were grown for 24 h in the liquid culture (SDCAA, 30°C, 220 rpm) and the yeast expression proceeded for 48 h at 20°C in 1/9 media. Expressed yeasts were washed with PBS supplemented with bovine serum albumin at a concentration of 1 g/l (PBSB). The cells were then exposed to a range of mACE2 concentrations (4 pM to 10 nM, in a dilution series with a factor of 2) and 20 nM bilirubin (Sigma-Aldrich, Cat# 14370-1G), washed with PBSB and the recorded data included RBD expression and ACE2 signal, captured using automated acquisition from 96-well plates by the FACS CytoFLEX Flow Cytometer (Beckman Coulter). Background binding signals were subtracted, and fluorescence spill of eUnaG2 signals into the red channel was compensated. Subsequently, the data were fitted to a standard noncooperative Hill equation through nonlinear least-squares regression, utilizing Python v3.7 (https://www.python.org) as previously detailed.[2,10,14,18,23,39,53]

Pseudovirus infection

Pseudovirus infection (Figure 2B) was performed as previously described.[21,29,35,32,54–56] Briefly, lentivirus (HIV-1)-based, luciferase-expressing reporter viruses were pseudotyped with the SARS-CoV-2 S protein. One prior day of transfection, the LentiX-293T or HEK293T cells were seeded at a density of 2×10^6 cells. The LentiX-293T or HEK293T cells were cotransfected with 1 μg psPAX2-IN/HiBiT (a packaging plasmid encoding the HiBiT-tag-fused integrase,[37] 1 μg pWPI-Luc2 (a reporter plasmid encoding a firefly luciferase gene[37] and 500 ng plasmids expressing parental S protein or its derivatives using TransIT-293 transfection reagent (Mirus, Cat# MIR2704) or TransIT-LT1 (Takara, Cat# MIR2300) according to the manufacturer's protocol. Two days posttransfection, the culture supernatants were harvested and filtrated. The amount of produced pseudovirus particles was quantified by the HiBiT assay using the Nano Glo HiBiT lytic detection system (Promega, Cat# N3040) as previously described.[37] In this system, HiBiT peptide is produced with HIV-1 integrase and forms NanoLuc luciferase with LgBiT, which is supplemented with substrates. In each pseudovirus particle, the detected HiBiT value is correlated with the amount of the pseudovirus capsid protein, HIV-1 p24 protein.[37] Therefore, we calculated the amount of HIV-1 p24 capsid protein based on the HiBiT value measured, according to the previous paper.[37] To measure viral infectivity, the same amount of pseudovirus normalized with the HIV-1 p24 capsid protein was inoculated into HOS-ACE2/TMPRSS2 cells. At 2 d.p.i., the infected cells were lysed with a Bright-Glo luciferase assay system (Promega, Cat# E2620), and the luminescent signal produced by firefly luciferase reaction was measured using a GloMax explorer multimode microplate reader 3500 (Promega) or CentroXS3 LB960 (Berthold Technologies). The pseudoviruses were stored at –80°C until use.

Western blotting

As previously described, sample preparation for western blotting was performed with minor modifications.[16,57] For western blotting, HEK293T cells (2×10^6 cells) were cotransfected with 2 μg of psPAX2-IN/HiBiT, 2 μg of pWPI-Luc2, and 1 μg of plasmids expressing SARS-CoV-2 S using TransIT-LT1 according to the manufacturer's protocol. At 2 d posttransfection, cell culture supernatants were collected, filtered, and subjected to ultracentrifugation using 20% sucrose (22,000 × *g*, 4°C, 2 h). Then, virions were dissolved in phosphate-buffered saline (PBS). To quantify HIV-1 p24 antigen in the pseudovirus, the amount of pseudoviruses in the cell culture supernatant was quantified by the HiBiT assay using a Nano Glo HiBiT lytic detection system (Promega, Cat# N3040). After normalization with HiBiT value, the samples were diluted with 2 × SDS sample buffer [100 mM Tris-HCl (pH6.8), 4% SDS, 12% β- mercaptoethanol, 20% glycerol, 0.05% bromophenol blue] and boiled for 5–10 minutes at 100°C. For cell lysate preparation, the transfected cells were detached, washed twice with PBS, and lysed in lysis buffer [25mM HEPES (pH7.2), 20% glycerol, 125 mM NaCl, 1% Nonidet P40 substitute (Nacalai Tesque, Cat# 18558-54), protease inhibitor cocktail (Nacalai Tesque, Cat# 03969-21)]. Quantification of total protein in the cell lysates was done by protein assay dye (Bio-Rad, Cat# 5000006) according to manufacturer's instruction. Then, cell lysates were diluted with 2 × SDS sample buffer and boiled for 5–10 minutes. After cooling down, viral (pseudovirus) and cell lysates were mixed with diluted sample buffer (proteinsimple, Cat# 99351). Then, 5 × Fluorescent Master mix (proteinsimple, Cat# PS-ST01EZ-8) was added at a ratio of 4:1. Simple Western System, Abby (proteinsimple) was used for protein analysis. For protein detection, the following antibodies were used: rabbit anti-SARS-CoV-2 S polyclonal antibody (Novus Biologicals, Cat# NB100-56578, viral lysate; 1:40, cell lysate; 1:40). mouse anti-HIV-1 p24 monoclonal antibody (HIV Reagent Program, ARP-3537, 1:500), mouse anti-α tubulin monoclonal antibody (Sigma-Aldrich, Cat# T5168, 1:100), anti-rabbit secondary antibody (proteinsimple, Cat# 042-206), and anti-mouse secondary antibody (proteinsimple, Cat# 042-205). Bands were visualized and analyzed using Compass for Simple Western v6.1.0 (proteinsimple).

SARS-CoV-2 S-based fusion assay

A SARS-CoV-2 S-based fusion assay (Figures 2D, S2D, and S2E) was performed as previously described.[10,11,15–18,21–23,29,58] Briefly, on day 1, effector cells (i.e., S-expressing cells) and target cells (Calu-3/DSP_{1-7} cells) were prepared at a density of 0.6–0.8 × 10^6 cells in a 6-well plate. On day 2, for the preparation of effector cells, HEK293 cells were cotransfected with the S expression plasmids (400 ng) and $pDSP_{8-11}$[38] (400 ng) using TransIT-LT1 (Takara, Cat# MIR2300). On day 3 (24 h posttransfection), 16,000 effector cells were detached and reseeded into a 96-well black plate (PerkinElmer, Cat# 6005225), and target cells were reseeded at a density of 1,000,000 cells/2 ml/well in 6-well plates. On day 4 (48 h posttransfection), target cells were incubated with EnduRen live cell substrate (Promega, Cat# E6481) for 3 h and then detached, and 32,000 target cells were added to a 96-well plate with effector cells. *Renilla* luciferase activity was measured at the indicated time points using Centro XS3 LB960 (Berthhold Technologies). For measurement of the surface expression level of the S protein, effector cells were stained with rabbit anti-SARS-CoV-2 S S1/S2 polyclonal antibody (Thermo Fisher Scientific, Cat# PA5-112048, 1:100). Normal rabbit IgG (Southern Biotech, Cat# 0111-01, 1:100) was used as a negative control, and APC-conjugated goat anti-rabbit IgG polyclonal antibody (Jackson ImmunoResearch, Cat# 111-136-144, 1:50) was used as a secondary antibody. The surface expression level of S proteins (Figure S2D) was measured using CytoFLEX Flow Cytometer (Beckman Coulter) and the data were analyzed using FlowJo software v10.7.1 (BD Biosciences). For calculation of fusion activity, *Renilla* luciferase activity was normalized to the mean fluorescence intensity (MFI) of surface S proteins. The normalized value (i.e., *Renilla* luciferase activity per the surface S MFI) is shown as fusion activity.

SARS-CoV-2 preparation and titration

The working virus stocks of SARS-CoV-2 were prepared and titrated as previously described.[10,11,15,18,19,21–23,29,35] In this study, clinical isolates of BA.2.86 (strain TKYnat15020; GISAID ID: EPI_ISL_18233521), EG.5.1 (strain KU2023071028; GISAID ID: EPI_ISL_18072016),[18] and BA.2 (strain TY40-385; PANGO lineage BA.2, GISAID ID: EPI_ISL_9595859)[22] were used. The working virus stocks of BA.2 and EG.5.1 were prepared in our previous studies.[18,22] To prepare the working virus stock of BA.2.86, 100 μl of the seed virus was inoculated into VeroE6/TMPRSS2 cells (1,000,000 cells in a one-well of 6-well plate). After 1 h absorption, the cells were cultured with DMEM (low glucose) (Fujiflim Wako, Cat# 041-29775) containing 2% FBS and 1% PS. At 3 d.p.i., the culture medium was harvested and then, subjected to inoculation into the naïve Vero/E6/TMPRS2 cells (10,000,000 cells in a 100-mm culture dish). After 84 h.p.i, the culture medium was harvested and centrifuged. The resultant supernatants were collected as the working virus stock.

The titer of the prepared working virus was measured as the 50% tissue culture infectious dose ($TCID_{50}$). Briefly, one day before infection, VeroE6/TMPRSS2 cells (10,000 cells) were seeded into a 96-well plate. Serially diluted virus stocks were inoculated into the cells and incubated at 37°C for 4 d. The cells were observed under a microscope to judge the CPE appearance. The value of $TCID_{50}$/ml was calculated with the Reed–Muench method.[59]

For verification of the sequences of SARS-CoV-2 working viruses, viral RNA was extracted from the working viruses using a QIAamp viral RNA mini kit (Qiagen, Cat# 52906) and viral genome sequences were analyzed as described above (see "viral genome sequencing" section). Information on the unexpected substitutions detected is summarized in Table S4 and the raw data are deposited in the GitHub repository (https://github.com/TheSatoLab/BA.2.86_full1).

SARS-CoV-2 infection

One day before infection, Vero cells (10,000 cells), VeroE6/TMPRSS2 cells (10,000 cells), and Calu-3 cells (10,000 cells) were seeded into a 96-well plate. SARS-CoV-2 [100 $TCID_{50}$ for VeroE6/TMPRSS2 cells (Figure 3A) and Vero cells (Figure 3B) and] was inoculated and incubated at 37°C for 1 h. The infected cells were washed, and 180 μl culture medium was added. The culture supernatant (10 μl) was harvested at the indicated timepoints and used for RT–qPCR to quantify the viral RNA copy number (see "RT-qPCR" section below).

Immunofluorescence staining

Immunofluorescence staining (Figure 3B) was performed as previously described.[19,21] In brief, one day before infection, VeroE6/TMPRSS2 cells (10,000 cells) were seeded into 96-well, glass bottom, black plates and infected with SARS-CoV-2 (100 $TCID_{50}$). At 72 h.p.i., the cells were fixed with 4% para- formaldehyde in phosphate-buffered saline (PBS) (Nacalai Tesque, 09154-85) for 1 h at 4 °C. The fixed cells were permeabilized with 0.2% Triton X-100 in PBS for 1 h and blocked with 10% FBS in PBS for 1 h at 4 °C. The fixed cells were then stained using rabbit anti-SARS-CoV-2 N poly-clonal antibody (GeneTex, GTX135570, 1:1,000) for 1 h. After washing three times with PBS, cells were incubated with an Alexa 488-conjugated anti-rabbit IgG antibody (Thermo Fisher Scientific, A-11008, 1:1,000) for 1 h. Fluorescence microscopy was performed on an All-in-One Fluorescence Microscope BZ-X800 (Keyence). Captured images were reconstructed and the fluorescent intensity was measured by using a BZ-X800 Analyzer software (Keyence).

RT–qPCR

RT–qPCR was performed as previously described.[10,11,15,17–19,21–23,34,29] Briefly, 5 μl culture supernatant was mixed with 5 μl 2 × RNA lysis buffer [2% Triton X-100 (Nacalai Tesque, Cat# 35501-15), 50 mM KCl, 100 mM Tris-HCl (pH 7.4), 40% glycerol, 0.8 U/μl recombinant RNase inhibitor (Takara, Cat# 2313B)] and incubated at room temperature for 10 m. RNase-free water (90 μl) was added, and the diluted sample (2.5 μl) was used as the template for real-time RT-PCR performed according to the manufacturer's protocol using One Step TB Green PrimeScript PLUS RT-PCR kit (Takara, Cat# RR096A) and the following primers: Forward *N*, 5'-AGC CTC TTC TCG TTC CTC ATC AC-3'; and Reverse *N*, 5'-CCG CCA TTG CCA GCC ATT C-3'. The viral RNA copy number was standardized with a SARS-CoV-2 direct detection RT-qPCR kit (Takara, Cat# RC300A). Fluorescent signals were acquired using QuantStudio 3 Real-Time PCR system (Thermo Fisher Scientific), CFX Connect Real-Time PCR Detection system (Bio-Rad), Eco Real-Time PCR System (Illumina), qTOWER3 G Real-Time System (Analytik Jena) or 7500 Real-Time PCR System (Thermo Fisher Scientific).

Airway-on-a-chip

Airways-on-a-chip (Figures 3G and 3H) were prepared as previously described.[20] Human lung microvascular endothelial cells (HMVEC-L) were obtained from Lonza (Cat# CC-2527) and cultured with EGM-2-MV medium (Lonza, Cat# CC-3202). For preparation of the airway-on-a-chip, the bottom channel of a polydimethylsiloxane (PDMS) device was first precoated with fibronectin (3 μg/ml, Sigma-Aldrich, Cat# F1141). The microfluidic device was generated according to our previous report.[60] HMVEC-L cells were suspended at 5,000,000 cells/ml in EGM2-MV medium. Then, 10 μl of suspension medium was injected into the fibronectin-coated bottom channel of the PDMS device. The PDMS device was turned upside down and incubated. After 1 h, the device was turned over, and EGM2-MV medium was added into the bottom channel. After 4 d, airway organoids (AO) were dissociated and seeded into the top channel. AOs were generated according to our previous report.[25] AOs were dissociated into single cells and then suspended at 5,000,000 cells/ml in the AO differentiation medium. Ten microliters of suspension medium were injected into the top channel. After 1 h, the AO differentiation medium was added to the top channel. In the infection experiments (Figures 3G and 3H), the AO differentiation medium, containing either BA.2, EG.5.1, and BA.2.86 isolate (500 $TCID_{50}$), was inoculated into the top channel. At 2 h.p.i., the top and bottom channels were washed and cultured with AO differentiation and EGM2-MV medium, respectively. The culture supernatants were collected, and viral RNA was quantified using RT-qPCR (see "RT-qPCR" section).

Microfluidic device

A microfluidic device was generated according to our previous report.[60] Briefly, the microfluidic device consisted of two layers of microchannels separated by a semipermeable membrane. The microchannel layers were fabricated from PDMS using a soft lithographic method. PDMS prepolymer (Dow Corning, Cat# SYLGARD 184) at a base-to-curing agent ratio of 10:1 was cast against a mold composed of SU-8 2150 (MicroChem, Cat# SU-8 2150) patterns formed on a silicon wafer. The cross-sectional size of the microchannels was 1 mm in width and 330 μm in height. Access holes were punched through the PDMS using a 6-mm biopsy punch (Kai Corporation, Cat# BP-L60K) to introduce solutions into the microchannels. Two PDMS layers were bonded to a PET membrane containing 3.0-μm pores (Corning, Cat# 353091) using a thin layer of liquid PDMS prepolymer as the mortar. PDMS prepolymer was spin-coated (4000 rpm for 60 sec) onto a glass slide. Subsequently, both the top and bottom channel layers were placed on the glass slide to transfer the thin layer of PDMS prepolymer onto the embossed PDMS surfaces. The membrane was then placed onto the bottom layer and sandwiched with the top layer. The combined layers were left at room temperature for 1 d to remove air bubbles and then placed in an oven at 60°C overnight to cure the PDMS glue. The PDMS devices were sterilized by placing them under UV light for 1 h before cell culture.

Antiviral drug assay using SARS-CoV-2 clinical isolates and human iPSC-derived lung organoids

Antiviral drug assay (Figure 3I) was performed as previously described.[35] The human iPSC-derived lung organoids (see "human lung organoids" section above) were infected with either BA.2, EG.5.1, or BA.2.86 isolate (100 $TCID_{50}$) at 37 °C for 2 h. The cells were washed with DMEM and cultured in DMEM supplemented with 10% FCS, 1% PS and the serially diluted EIDD-1931 (an active metabolite of Molnupiravir; Cell Signalling Technology, Cat# 81178S), Nirmatrelvir (PF-07321332; MedChemExpress, Cat# HY-138687), Remdesivir (Clinisciences, Cat# A17170), or Ensitrelvir (MedChemExpress, Cat# HY-143216). At 72 h after the infection, the culture supernatants were collected, and viral RNA was quantified using RT–qPCR (see "RT-qPCR" section above). The assay of each compound was performed in triplicate, and the 50% effective concentration (EC_{50}) was calculated using Prism 9 software v9.1.1 (GraphPad Software).

Lung function test

Lung function test (Figure 4A) was performed every day as previously described.[10,11,15,17–19,21–23] Respiratory parameters (Penh and Rpef) were measured by using a whole-body plethysmography system (DSI) according to the manufacturer's instructions. In brief, a hamster was placed in an unrestrained plethysmography chamber and allowed to acclimatize for 30 seconds, then, data were acquired over a 2.5-minute period by using FinePointe Station and Review softwares v2.9.2.12849 (DSI).

Immunohistochemistry

Immunohistochemistry (IHC) (Figures 4C, S3A, and S3B) was performed as previously described[10,11,15,19,21–23] using an Autostainer Link 48 (Dako). The deparaffinized sections were exposed to EnVision FLEX target retrieval solution high pH (Agilent, Cat# K8004) for 20 minutes at 97°C for activation, and a mouse anti-SARS-CoV-2 N monoclonal antibody (clone 1035111, R&D Systems, Cat# MAB10474-SP, 1:400) was used as a primary antibody. The sections were sensitized using EnVision FLEX for 15 minutes and visualized by peroxidase-based enzymatic reaction with 3,3′-diaminobenzidine tetrahydrochloride (Dako, Cat# DM827) as substrate for 5 minutes. The N-protein positivity was evaluated by certificated pathologists as previously described. Images were incorporated as virtual slides by NDP.scan software v3.2.4 (Hamamatsu Photonics). The N-protein positivity was measured as the area using Fiji software v2.2.0 (ImageJ).

H&E staining

H&E staining (Figures 4D, S4A, and S4B) was performed as previously described.[10,11,15,19,21–23] Briefly, excised animal tissues were fixed with 10% formalin neutral buffer solution and processed for paraffin embedding. The paraffin blocks were sectioned at a thickness of 3 μm and then mounted on MAS-GP-coated glass slides (Matsunami Glass, Cat# S9901). H&E staining was performed according to a standard protocol.

Histopathological scoring

Histopathological scoring (Figure 4E) was performed as previously described.[10,11,15,19,21–23] Pathological features, including (i) bronchitis or bronchiolitis, (ii) hemorrhage with congestive edema, (iii) alveolar damage with epithelial apoptosis and macrophage infiltration, (iv) hyperplasia of type II pneumocytes, and (v) the area of hyperplasia of large type II pneumocytes, were evaluated in each hamsters by certified pathologists, and the degree of these pathological findings was arbitrarily scored using a four-tiered system as 0 (negative), 1 (weak), 2 (moderate), and 3 (severe). The "large type II pneumocytes" are type II pneumocytes with hyperplasia exhibiting more than 10-μm-diameter nuclei. We described "large type II pneumocytes" as one of the notable histopathological features of SARS-CoV-2 infection in our previous studies. The total histological score is the sum of these five indices.

QUANTIFICATION AND STATISTICAL ANALYSIS

Statistical significance was tested using a two-sided Mann–Whitney *U* test, a two-sided Student's *t* test, a two-sided Welch's *t* test, or a two-sided paired *t*-test unless otherwise noted. The tests above were performed using Prism 9 software v9.1.1 (GraphPad Software).

In the time-course experiments (Figures 2D, 3A, 3C–3G, 4A–4E, and S2F), a multiple regression analysis including experimental conditions (i.e., the types of infected viruses) as explanatory variables and timepoints as qualitative control variables was performed to evaluate the difference between experimental conditions thorough all timepoints. The initial time point was removed from the analysis. The *P* value was calculated by a two-sided Wald test. Subsequently, familywise error rates (FWERs) were calculated by the Holm method. These analyses were performed in R v4.1.2 (https://www.r-project.org/).

In Figure 3B, photographs shown are the representatives of 57 fields of view taken for each sample of at least two independent experiments.

In Figures 4C, 4D, S3, and S4, photographs shown are the representative areas of at least two independent experiments by using four hamsters at each timepoint.